TURUN YLIOPISTO
UNIVERSITY OF TURKU

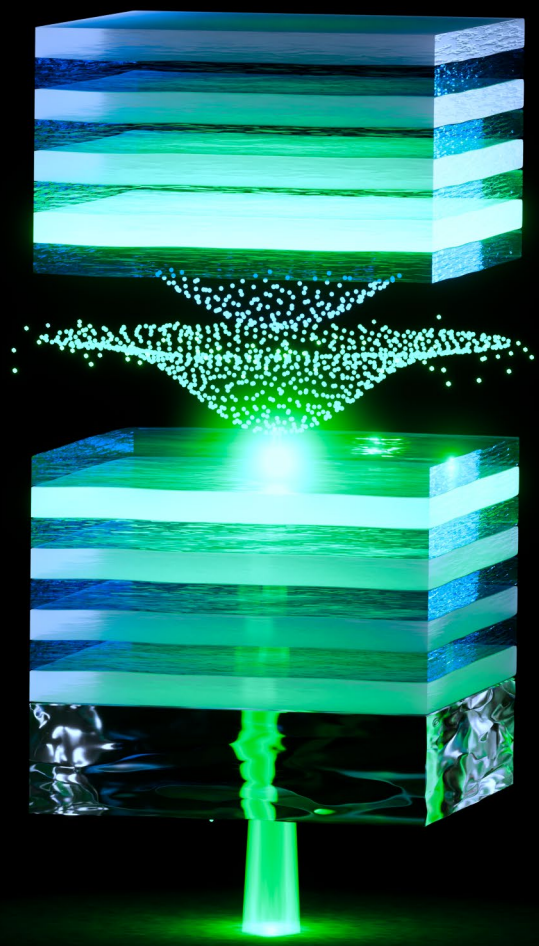

Microcavity Engineering for Scalable, Efficient Polaritonic Applications

Hassan Ali Qureshi

TURUN YLIOPISTON JULKAISUJA – ANNALES UNIVERSITATIS TURKUENSIS
SARJA – SER. F OSA – TOM. 81 | TECHNICA – INFORMATICA | TURKU 2026

TURUN
YLIOPISTO
UNIVERSITY
OF TURKU

MICROCAVITY ENGINEERING FOR SCALABLE, EFFICIENT POLARITONIC APPLICATIONS

Hassan Ali Qureshi

TURUN YLIOPISTON JULKAISUJA ANNALES UNIVERSITATIS TURKUENSIS
SARJA SER. F OSA TOM. 81 | TECHNICA INFORMATICA | TURKU 2026

University of Turku

Faculty of Technology
Department of Mechanical and Meterials Engineering
Materials Engineering
Doctoral programme in Technology

Supervised by

Assoc. Prof., Konstantinos Daskalakis
University of Turku
Turku, Finland

PhD, Emilia Palo
University of Turku
Turku, Finland

Reviewed by

Professor, Arri Priimägi
Tampere University

Assoc. Prof., Nicolo Maccaferri
Umeå University

Opponent

Assoc. Prof., Grigorios Itskos
University of Cyprus

ISBN 978-952-02-0621-5 (PRINT)
ISBN 978-952-02-0622-2 (PDF)
ISSN 2736-9390 (PRINT)
ISSN 2736-9684 (ONLINE)
Painosalama, Turku, Finland, 2026

To Allah – the source of all knowledge in universe
To my beloved Mother (May her soul rest in heaven) and Father for lifelong support, love and prayers
To my beloved wife Kanza for her unconditional love and sacrifices
To my adorable children, Hafi and Faris "I hope you will be always proud of baba"
To my wonderful siblings Fatima, Urwah and Talha "I know you are proud of me"

UNIVERSITY OF TURKU
Faculty of Technology
Department of Mechanical and Meterials Engineering
Materials Engineering
QURESHI, HASSAN ALI: Microcavity Engineering for Scalable, Efficient Polaritonic Applications
Doctoral dissertation, 134 pp.
Doctoral programme in Technology
April 2026

ABSTRACT

Optical microcavities provide a powerful platform for tailoring light–matter interaction through optical confinement, spectral selectivity, and electromagnetic field enhancement. When combined with organic semiconductors, microcavities enable spectral narrowing, angle-dependent dispersion, and, in the strong coupling regime, the formation of exciton-polaritons, hybrid light-matter quasiparticles with low effective mass and high spatial delocalization. The performance and scalability of polaritonic systems therefore depend critically on microcavity design and fabrication.

This dissertation investigates microcavity engineering for scalable polaritonic applications using solution-processed and vacuum-fabricated architectures. The fundamental principles of optical confinement in planar microcavities are established, providing a framework for understanding confined light-matter interaction.

Strong coupling and exciton-polariton formation are demonstrated in hybrid and fully solution-processed dielectric distributed Bragg reflector microcavities fabricated by dip-coating and spin-coating. An automated deposition approach enables reproducible multilayer control, yielding microcavities with quality factors exceeding 200 using a limited number of DBR pairs. Angle-resolved reflectivity and photoluminescence measurements reveal clear anticrossing behavior and large Rabi splittings. Under non-resonant optical excitation above a critical pump fluence of approximately 20 $\mu \mathrm{J} cm^{-2}$, these microcavities exhibit nonlinear emission and room-temperature polariton lasing.

The thesis also examines polaritonic microcavity engineering in vacuum-fabricated organic light-emitting diode architectures. Time-resolved electroluminescence measurements show that delayed emission is dominated by trap-assisted processes, indicating negligible influence of polaritons on intramolecular excited-state dynamics. Microcavity and surface plasmon polariton mode engineering further enable spectral and color control, yielding single-emitter, top-emitting white OLEDs with tunable color temperature.

Overall, this work demonstrates microcavity engineering as a viable strategy for scalable polariton physics and practical optoelectronic devices.

KEYWORDS: organic polaritons; solution-processed microcavities.

TURUN YLIOPISTO
Teknillinen tiedekunta
Kone- ja materiaalitekniikan laitos
Materiaalitekniikka
QURESHI, HASSAN ALI: Microcavity Engineering for Scalable, Efficient Polaritonic Applications
Väitöskirja, 134 s.
Teknologian tohtoriohjelma
Huhtikuu 2026

TIIVISTELMÄ

Optiset mikrokaviteetit tarjoavat tehokkaan alustan valon ja aineen vuorovaikutuksen muokkaamiseen optisen rajoittamisen, spektrisen selektiivisyyden ja sähkömagneettisen kentän vahvistamisen avulla. Yhdistettynä orgaanisiin puolijohteisiin mikrokaviteetit mahdollistavat spektrin kaventumisen, kulmariippuvan dispersion sekä vahvan kytkennän alueella eksitoni-polaritoniparien muodostumisen. Eksitoni-polaritonit ovat valon ja aineen hybridi-kvasihiukkasia, joille on ominaista pieni efektiivinen massa ja suuri spatiaalinen delokalisaatio. Polaritonijärjestelmien suorituskyky ja skaalautuvuus riippuvat siten ratkaisevasti mikrokaviteettien suunnittelusta ja valmistuksesta. Tässä väitöskirjassa tutkitaan mikrokaviteettitekniikkaa skaalautuvia polaritonisovelluksia varten hyödyntäen liuosprosessointiin perustuvia sekä tyhjiövalmistettuja rakenteita. Tasomaisten mikrokaviteettien optisen rajoittumisen perusperiaatteet esitetään, ja muodostetaan viitekehys valon ja aineen vuorovaikutuksen ymmärtämiselle. Vahva kytkentä ja eksitoni-polaritonien muodostuminen osoitetaan hybridi- ja täysin liuosprosessoiduissa dielektrisissä Braggin heijastinmikrokaviteeteissa, jotka on valmistettu upotus- ja pyöröpinnoitus-menetelmillä. Automatisoitu pinnoitusmenetelmä mahdollistaa toistettavan monikerrosrakenteen hallinnan, ja saavutetut mikrokaviteetit saavuttavat yli 200:n laatukertoimen rajallisella määrällä DBR-parikerroksia. Kulmariippuvaiset heijastus- ja fotoluminesenssimittaukset osoittavat suuren Rabi-jakautumisen ja selkeän erotuksen polaritonienergioissa, jotka eivät leikkaa keskenään. Epäresonanttisessa optisessa pumppauksessa, kriittisen noin $20\,\mu\mathrm{J\ cm^{-2}}$ pumppausfluenssin yläpuolella, mikrokaviteetit osoittavat epälineaarista emissiota ja mahdollistavat huoneenlämpöisen laser-käyttäytymisen polaritoneissa. Väitöskirjassa tarkastellaan lisäksi polaritonisten mikrokaviteettien suunnittelua tyhjiövalmistetuissa orgaanisissa OLED-rakenteissa. Aikaerotteiset elektroluminesenssimittaukset osoittavat, että viivästynyt emissio on pääosin ansa-avusteisten prosessien hallitsemaa, mikä viittaa siihen, että polaritoneilla on vähäinen vaikutus molekyylin sisäiseen virittyneiden tilojen dynamiikkaan. Mikrokaviteetti- ja pintaplasmonipolaritonimoodien suunnittelu mahdollistaa spektrin ja värin hallinnan, ja tuloksena saavutetaan yhtä emittoivaa materiaalia käyttäviä, yläemissiivisiä valkoisia OLED-rakenteita säädettävällä värilämpötilalla. Kokonaisuutena tämä työ osoittaa, että mikrokaviteettitekniikka tarjoaa toteuttamiskelpoisen strategian skaalautuvalle polaritonifysiikalle ja käytännöllisille optoelektronisille laitteille.

ASIASANAT: orgaaniset polaritoni; liuosprosessoidut mikrokaviteetit.

Acknowledgements

First of all, praises and gratitude to Allah who is merciful and beneficiant, who has given me strength, courage and tiny portion of knowledge to complete this thesis.

I am deeply grateful to my supervisor, Dr. Konstantinos S. Daskalakis, for his guidance, trust, and unwavering support throughout my doctoral studies. From the very beginning of my PhD, he spent considerable time with me in the laboratory, patiently teaching me the fundamentals of optical spectroscopy and experimental techniques that became central to my research. His insights, encouragement, and confidence in my abilities shaped my scientific thinking and helped me grow as an independent researcher. To my second supervisor, Dr. Emilia Palo, for her support and helpful discussions during my doctoral studies, particularly for her advice regarding the development of solution-processed mirrors. To my former supervisors, Professor Jussi Toppari and Dr. Arpan Dutta, for their guidance and support during the earlier stages of my research journey. To my collaborators, Dr. Kimmo Luoma, Dr. Mikko Salomäki, and Dr. Antti J. Moilanen, for their collaboration and expertise, which significantly contributed to this work. To my pre-examiners, Professor Arri Priimagi and Associate Professor Nicolò Maccaferri-Martino, for their careful evaluation of this thesis and for their constructive comments and valuable suggestions.

I would like to thank my colleagues in the LMD group — Mike, Manish, Henri, Olli, Oskar, Santeri, Akseli N., Akseli K. and Malek — for many scientific and general discussions, for their help and support, and for the memorable moments we shared during this journey. To my colleagues in the department, Dr. Vipul Sharma, Mehboba, Rustam, and Rituporn, for their discussions and support. A special thanks goes to my friend, fellow doctoral researcher, and former colleague Ahmed for his constant encouragement, for sharing ideas, and for the many scientific discussions we had in the office, at conferences, in the lab, and during our walks. Ahmed, you have been like an older brother to me. Your ideas were always inspiring, and your presence was a constant source of motivation. I learned a great deal both with you and from you. Additionally, I would like to thank Magda and Matilde for their support, for listening, and for sharing this journey with me.

I am truly grateful to my friends and their respective families in Turku who made this journey more enjoyable and memorable. To Naman, for sharing his place where I could relax, release stress, enjoy delicious food, and always offering help whenever needed. To Adil, for always being there for me and for the many long discussions

we shared. To Zain, for constantly fueling optimism and for the delicious biryani. To Sheheryar M., for the late-night snooker sessions. And to Basit, Sheheryar T., Intikhab, Asim, Shafi bhai, Ikram, Jarar bhai for their support and for the many unforgettable moments we shared. Guys, without you I would not have been able to make it this far. Thank you!

I would also like to extend my gratitude to Haroon, A. Wahab, and Ghulam Hur — thank you for your immense support, love, and brotherhood. Having you in my life never made me feel alone.

A special thanks to Dr. Imran Qureshi for being a role model and a constant source of motivation, both on and off the field. Thank you for providing the right direction and guidance throughout my journey. I might not have reached this point without your presence and support. To Tuaha Sohail, for the support and for always offering the right suggestions when they were needed.

I would like to thanks my family. Maa jee, the word "thanks" is too small to express my gratitude for your lifelong sacrifices, prayers, support, and nurturing. I only wish that you were here to witness this moment. Abu jee, thank you for providing me with everything I needed, for making me independent, and for always believing in and supporting in every step of my journey. Fatima, thank you for being my first friend, my school partner, and a wonderful sister. Urwah and Talha, thank you for being such caring younger siblings, for taking care of everyone when I was away, and for shielding me from many worries so that I could focus on my work. Then a thanks to my extended family, my mother and father-in-law, Munazzah, Hajira, Ataullah, Nabiha, Rohina and Madiha for their prayers and support. Additionally, thanks to all my cousins, uncles, and aunts who supported me and kept me in their prayers.

Faris and Hafi, you are the greatest joy of my life. While I was working on this, you were growing, learning, and filling our home with happiness. I hope one day you read this and know that you were always my motivation. You can become anything you choose, but remember to never give up.

Kanza, I might not always have been a good husband, but you have been an amazing wife to me. I would not have been able to even complete my master's degree without you. Thank you for all the sacrifices you made, for your unconditional support and care, for managing everything when I could not, and for bearing my stress-induced silence and absence. Thank you for standing by me in both the good and the difficult times. You have filled my life with love, joy, and two beautiful children. I am proud to have you by my side and this PhD is equally yours.

Finally, I gratefully acknowledge UTU Graduate School funding, Finnish Cultural Foundation and Magnus Ehrnrooth Foundation for supporting my PhD.

16.03.2026
Hassan Ali Qureshi

Table of Contents

Abbreviations

UP	Upper polariton
LP	Lower polariton
MP	Middle polariton
SC	Strong coupling
DBR	Distributed Bragg reflectors
ISC	Intersystem crossing
OLED	Organic light emitting diode
POLED	Polaritonic organic light emitting diode
VCSEL	Vertical cavity surface emitting laser
TMM	Transfer matrix method
TiOH	Titanium hydroxide
PVA	Polyvinyl alcohol
PS	Polystyrene
HOMO	Highest occupied molecular orbital
LUMO	Lowest unoccupied molecular orbital
PLQY	Photoluminescence quantum yield
Ex	Exciton
S_0	Ground state
S_1	Excited singlet state
T_1	Triplet state
PL	Photoluminescence
EL	Electroluminescence
TADF	Thermally activated delayed fluorescence
RISC	Reverse intersystem crossing
LDOS	Local density of optical states
CHO	Coupled harmonic oscillators
FWHM	Full width at half maximum
SPP	Surface plasmon polaritons
DPAVB	4-(Di-p-tolylamino)-4'-[(di-p-tolylamino)styryl]stilbene
R6G	Rhodamine 6G
TDAF	2,7-Bis[9,9-di(4-methylphenyl)-fluoren-2-yl]-9,9-di(4 methylphenyl)fluorene
DMAC-DPS	10,10'-(4,4'-Sulfonylbis(4,1-phenylene))bis(9,9-dimethyl-9,10- -dihydroacridine)

λ_{dB}	de Broglie wavelength
HIL	Hole-injection layer
HTL	Hole-transport layer
EML	Emissive layer
ETL	Electron-transport layer
EIL	Electron-injection layer
IQE	Internal quantum efficiency
EQE	External quantum efficiency
AO	Atomic orbital
MO	Molecular orbital
TTA	Triplet–triplet annihilation
TE	Trap emission
ITO	Indium tin oxide
BFP	Back focal plane
NA	Numerical aperture
FF	Far field
OPA	Optical parametric amplification
CCD	Charge coupled device
APD	Avalanche photodiode

List of Original Publications

This dissertation is based on the following original publications, which are referred to in the text by their Roman numerals:

I Emilia Palo, Michael A. Papachatzakis, Ahmed Gaber Abdelmagid, **Hassan A. Qureshi**, Manish Kumar, Mikko Salomäki, and Konstantinos S. Daskalakis. "Developing solution-processed distributed Bragg refectors for microcavity polariton applications". The Journal of Physical Chemistry C, 2023; 127(29):14255–14262.

II **Hassan A. Qureshi**, Michael A. Papachatzakis, Ahmed Gaber Abdelmagid, Mikko Salomäki, Ermei Mäkilä, Oskar Tuomi, Olli Siltanen, and Konstantinos S. Daskalakis. "Giant Rabi Splitting and Polariton Photoluminescence in an all Solution-Deposited Dielectric Microcavity". Advanced Optical Materials, 2025; 13(16):2500155.

III **Hassan A. Qureshi**, Henri Lyyra, Akseli Korkeamäki, Oskar Tuomi, Antti J. Moilanen, and Konstantinos S. Daskalakis. "A fully solution-processed organic microcavity laser in the strong light–matter coupling regime". Manuscirpt under review, 2025

IV Ahmed Gaber Abdelmagid, **Hassan A. Qureshi**, Michael A. Papachatzakis, Olli Siltanen, Manish Kumar, Ajith Ashokan, Seyhan Salman, Kimmo Luoma, and Konstantinos S. Daskalakis. "Identifying the origin of delayed electroluminescence in a polariton organic light-emitting diode". Nanophotonics, 2024; 14: 2565-2573.

V Manish Kumar, Arpan Dutta, **Hassan A. Qureshi**, Michael A. Papachatzakis, Ahmed Gaber Abdelmagid, Konstantinos S. Daskalakis. "Single-Emitter White OLEDs via Microcavity Spectral Engineering." Advanced Optical Materials, 2025 ; 13(28).

Publications produced but not included in this doctoral thesis:

I Timo Leppälä, Ahmed Gaber Abdelmagid, **Hassan A. Qureshi**, Konstantinos S. Daskalakis, and Kimmo Luoma. "Linear optical properties of organic microcavity polaritons with non-Markovian quantum state diffusion." Nanophotonics, vol. 13, no. 14, 2024, pp. 2479-2490.

II Ahmed Gaber Abdelmagid, Zhuoran Qiao, Boudewijn Coenegracht, Gaon Yu, **Hassan A. Qureshi**, Thomas D. Anthopoulos, Nicola Gasparini, and Konstantinos S. Daskalakis "Polaritons in Non-Fullerene Acceptors for High Responsivity Angle-Independent Organic Narrowband Infrared Photodiodes." Advanced Optical Materials, 2025 ; 13(28): e01727.

Declaration of AI use

In preparing this dissertation, generative AI tools (ChatGPT and Grammarly) were used solely for grammar, spelling, readability, and LaTeX formatting. No AI was used to develop research ideas, analyse data, or draw conclusions.

1 Introduction

Light plays a central role in shaping our world and enabling technologies that underpin modern society. Through its interaction with matter, it governs phenomena ranging from vision and photosynthesis to optical communication and quantum information processing. The ability to confine and manipulate these interactions to harness inter-atomic and quantum mechanical effects is central to key technologies such as communication, sensing, energy, and displays [1]. Accessing these effects often requires confining the optical mode to micrometer-scale within a material structure, enabling an enhanced electromagnetic field. One of the simplest and most effective architectures for achieving this is the optical microcavity, consisting of two reflective mirrors separated by a distance on the order of the optical wavelength. These structures support standing electromagnetic waves, known as cavity modes, that can enable light–matter interactions. [2].

The conceptual understanding of light–matter interaction has evolved through a series of theoretical and experimental milestones. Classical electrodynamics was established in the nineteenth century with Maxwell's equations, which unified electricity, magnetism, and optics within a single framework and were later experimentally verified through the observation of electromagnetic waves [3, 4]. However, classical theory failed to explain phenomena such as blackbody radiation and the photoelectric effect, which led to the development of quantum theory in the early twentieth century. The introduction of energy quantization by Planck and the photon concept by Einstein laid the foundations of quantum mechanics [5, 6]. These ideas were later formalized in the quantum description of light–matter interaction through quantum electrodynamics [7, 8].

When an active material with electronic transitions is placed inside an optical microcavity, it interacts with the confined electromagnetic field. This interaction can be viewed as a coherent exchange of energy between cavity photons, representing the quantized electromagnetic field, and excitons, which are bound electron–hole pairs within the material. The interaction strength is governed by the transition dipole moment of the material and the effective mode volume of the cavity, which determines the degree of optical field confinement. In systems comprising many emitters, the coupling strength increases collectively as $\sqrt{N}$. At low interaction strengths, the system operates in the weak-coupling regime, where optical losses dominate and the cavity primarily modifies the emission rate and spectral distribution. When the rate of

coherent energy exchange between photons and excitons exceeds their respective loss rates, the system enters the strong-coupling regime, giving rise to new hybrid eigenstates known as exciton–polaritons [9–11]. These quasiparticles combine the low effective mass and coherence of photons with the interactions and nonlinear response of matter, enabling phenomena inaccessible in the weak-coupling regime, such as superfluidity and low-threshold lasing [1, 12]. More recently, strong coupling has been widely used to tailor the optical environment and the photonic density of states, enabling spectral reshaping (e.g., narrowing and angular redistribution) and modified emission characteristics without necessarily altering the underlying molecular relaxation pathways [13]. The theoretical foundations of coherent light–matter interaction were established by Jaynes and Cummings in 1963, who described reversible energy exchange between a quantized field and a two-level system [14]. Early experimental demonstrations of this regime were achieved in atomic and inorganic solid-state systems [15–17]. The concept was subsequently extended to semiconductor microcavities, where exciton–polaritons were first observed in the early 1990s [9]. Strong coupling in organic materials was proposed by Agranovich in 1997 and experimentally realized shortly thereafter by Lidzey and co-workers, marking the emergence of organic polaritonics [11, 18]. Building on these developments, it was later shown that exciton–polaritons can undergo macroscopic occupation of a single quantum state, leading to polariton lasing. This regime was first realized in inorganic semiconductor microcavities at cryogenic temperatures and subsequently extended to wide-bandgap inorganic systems and organic microcavities operating at room temperature [19–22].

Organic semiconductors are particularly promising for strong coupling at room temperature due to their tightly bound Frenkel excitons with large oscillator strengths and high binding energies [23]. These properties allow the formation of stable polaritons at room temperature important for realizing practical devices [12, 22]. Moreover, organic materials offer molecular tunability of optical transitions and compatibility with low-cost, large-area, and solution-processed fabrication methods such as spin coating, dip coating, and printing. These properties make them suitable for next-generation photonic and optoelectronic devices that are energy-efficient and compatible with low-cost fabrication [24].

Despite these advantages, achieving strong coupling in organic systems has predominantly relied on vacuum-deposited microcavity architectures fabricated using sputtering, e-beam evaporation, or atomic layer deposition [11, 25, 26]. Such techniques produce high-reflectivity mirrors and excellent optical quality microcavities, but they are expensive, energy intensive, and sometimes incompatible with delicate organic emitters. In contrast, solution processed microcavities provide a low cost and scalable fabrication route. However, their optical quality, including reflectivity, layer uniformity, and interfacial smoothness, has generally remained insufficient for achieving strong coupling. Most reported solution-processed distributed Bragg reflectors (DBRs) exhibit reflectivities below about 90–95% and insufficient qual-

ity factors, which can limit achievable Rabi splittings and hinder the realization of polariton lasing [27]. More recently, Stingelin and co-workers have reported fully solution-processed microcavities in which both DBR mirrors and the active layer are fabricated from solution and that support clear signatures of strong light–matter coupling [28]. In parallel, Publication III demonstrates solution-processed polariton microcavities based on Rhodamine 6G, achieving Rabi splittings of up to 400 meV and highlighting the potential of fully solution-based architectures for accessing strong and ultra-strong coupling regimes. Nevertheless, when compared to work on vacuum-deposited semiconductor and microcavities, the number of demonstrations achieving robust, reproducible strong coupling and especially polariton lasing in fully solution-processed platforms remains relatively limited. This motivates the development of new solution-processed DBR architectures with carefully engineered refractive-index contrast, low scattering losses, and precise thickness control specifically tailored to strong-coupling and polariton-lasing applications.

This thesis addresses these limitations by developing and understanding solution-processed microcavities capable of supporting strong light–matter coupling in organic materials. Specifically, it introduces a scalable, ambient-processed DBR architecture based on solution-deposited multilayers that achieves optical quality and reflectivity comparable to sputtered DBRs [29]. This work enables strong coupling with large Rabi splittings and establishes a reproducible design, fabrication and characterization methodology for solution-processed microcavities, as reported in Publication II [30]. Building upon this platform, the thesis further investigates exciton–polariton behavior under different excitation regimes, including singlet–singlet annihilation (SSA) processes in Publication II and polariton lasing in Publication III.

In parallel, the thesis explores vacuum-deposited microcavity organic light-emitting diodes (OLEDs) to demonstrate how optical confinement can be used to tailor emission properties. Through controlled tuning of cavity detuning and mirror thickness, these devices exhibit spectral narrowing, color control, and enhanced outcoupling efficiency, as reported in Publication V [31]. The thesis also investigates how strong light–matter coupling modifies excitonic relaxation pathways. In particular, Publication IV addresses the important question of whether polaritonic states can enable triplet harvesting by altering intersystem crossing kinetics and opening new radiative channels [13, 32–39]. These results show that microcavity engineering provides a platform for studying both OLED performance and their underlying photophysical mechanisms.

Together, these studies form a comprehensive body of work that links microcavity design, fabrication techniques, strong coupling physics, and device performance, advancing the field toward accessible polaritonic systems. The thesis establishes solution-processed microcavities as a viable alternative to vacuum-based approaches and provides a framework for engineering optical modes in both polaritonic devices and OLED architectures.

2 Optical microcavities

Note: The DBR architectures and fabrication strategies described in this chapter are based on the work reported in Publications I–III, where solution-processed multilayer mirrors were developed and integrated into optical microcavity structures. Unless otherwise stated, the theoretical background and equations discussed in this chapter are based on standard formulations found in Refs. [40, 41].

Optical microcavities provide a controlled electromagnetic environment in which light can be confined, enhanced, and manipulated on sub-wavelength length scales. By restricting the propagation of photons between two parallel mirrors, these structures support discrete resonant modes whose energies and spatial profiles are determined by the optical path length of the cavity. The simplest realization is the Fabry–Pérot resonator, consisting of two reflective surfaces separated by a spacer layer, as illustrated in Figure 1. Multiple reflections within the cavity give rise to constructive interference at specific wavelengths, creating standing-wave modes with well-defined resonant conditions.

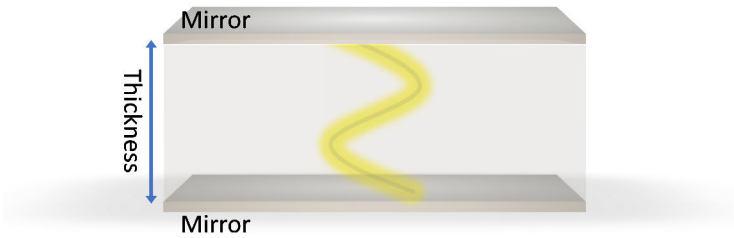

Figure 1. Schematic of a planar Fabry–Pérot microcavity showing two parallel mirrors separated by a cavity spacer of thickness d, with light confined between the mirrors.

Different mirror architectures give rise to distinct optical properties. Metal-clad microcavities, based on thin layers of metals such as silver, gold, or aluminum, offer simple fabrication and strong field confinement, but their performance is limited by absorption losses. In contrast, dielectric microcavities employ DBRs, a periodic stacks of alternating high- and low-refractive-index materials to achieve very high

reflectivity and low loss. These dielectric structures support sharper resonances and higher quality factors, making them particularly suitable for applications requiring precise spectral control, including vertical-cavity surface-emitting lasers (VCSELs), cavity-enhanced LEDs, and polaritonic devices [42, 43].

The aim of this chapter is to establish the theoretical framework required to understand the optical behavior of microcavities. We introduce the fundamental principles governing their resonant modes, the influence of mirror design on cavity quality, and the conditions under which light–matter interactions can be modified or enhanced. These concepts form the basis for the solution-processed microcavity architectures developed in Chapter 3 and for the strong-coupling phenomena discussed in subsequent chapters.

2.1 Optical confinement

In a planar microcavity, the electromagnetic field is confined in the direction perpendicular to the mirror surfaces, while photons remain free to propagate in the plane of the cavity. This vertical confinement leads to quantization of the photon field and the formation of discrete longitudinal optical modes. Constructive interference occurs when the optical path length between the mirrors corresponds to an integer multiple of half the wavelength of light inside the cavity medium. The resonance condition is therefore given by

$$\lambda_{\perp} = \frac{2n_c d_c}{m}, \tag{1}$$

where n_c is the effective refractive index of the cavity spacer, d_c is its physical thickness, and m is the longitudinal mode order ($m \geq 1$). This relation shows that the resonant wavelength can be tuned by adjusting either the cavity thickness or its refractive index.

Light confined within the cavity is described by a total wavevector k_{tot}, composed of components perpendicular ($k_{\perp}$) and parallel ($k_{\parallel}$) to the mirror surfaces,

$$k_{\text{tot}}^2 = k_{\perp}^2 + k_{\parallel}^2. \tag{2}$$

The perpendicular component is fixed by the boundary conditions imposed by the mirrors,

$$k_{\perp} = \frac{\pi m}{n_c d_c},$$

while the in-plane component is related to the propagation angle θ inside the cavity,

$$k_{\parallel} = k_{\text{tot}} \sin\theta.$$

This leads to an angle-dependent resonance condition for the cavity mode,

$$\lambda_c(\theta) = \frac{2n_c d_c \cos\theta}{m}. \tag{3}$$

Correspondingly, the cavity mode energy exhibits angular dispersion,

$$E_c(\theta) = \frac{hcm}{2n_c d_c \cos\theta} = \frac{E_0}{\cos\theta}, \tag{4}$$

where E_0 is the mode energy at normal incidence, h is Planck's constant, and c is the speed of light in vacuum. This angular dependence gives rise to the characteristic parabolic dispersion observed in angle-resolved reflectivity and photoluminescence measurements.

Experimentally, optical measurements are performed from outside the cavity. The internal and external angles are related by Snell's law,

$$n_c \sin\theta_{\text{int}} = n_{\text{ext}} \sin\theta_{\text{ext}}, \tag{5}$$

where n_{ext} is the refractive index of the surrounding medium (typically air, $n_{\text{ext}} = 1$).

Apart from spectral and angular properties of the cavity mode, spatial confinement also determines the strength of the vacuum electromagnetic field associated with a single photon. For a cavity mode of angular frequency ω_c, the root-mean-square vacuum electric field amplitude is given by

$$E_0 = \sqrt{\frac{\hbar\omega_c}{2\varepsilon_0 V}}, \tag{6}$$

where $\hbar\omega_c$ is the photon energy, ε_0 is the vacuum permittivity, and V is the effective mode volume of the cavity. This expression shows that the vacuum field strength increases for higher photon energies and, most critically, for stronger spatial confinement of the optical mode. In planar microcavities, the small cavity thickness and strong field localization at the antinode significantly enhance the electric field per photon.

The magnitude of the vacuum electric field directly governs the light–matter interaction strength with embedded emitters, such as molecular excitons. Strong field confinement, combined with a high density of optical oscillators, enables the collective interaction energy to exceed dissipative losses, forming the basis for strong coupling and polaritonic phenomena discussed in later chapters.

The overall strength of optical confinement can be quantified by the cavity quality factor (Q), defined as the ratio of the resonance wavelength to the spectral linewidth,

$$Q = \frac{\lambda}{\Delta\lambda}. \tag{7}$$

A high Q factor corresponds to a long photon lifetime and narrow linewidth, both of which are desirable for cavity-enhanced emission and polariton lasing. The achievable Q depends strongly on mirror reflectivity and absorption losses: metal mirrors typically yield $Q < 100$, whereas high-quality dielectric distributed Bragg reflectors can achieve Q values exceeding 10^3.

2.2 Fresnel reflection and multilayer optics

The interaction of light with planar microcavities is governed by reflection and transmission at interfaces between materials of different refractive indices. For a single planar interface between two non-absorbing media with refractive indices n_1 and n_2, the complex amplitude reflection coefficient at normal incidence is given by the Fresnel equation [40],

$$r = \frac{n_1 - n_2}{n_1 + n_2}, \qquad R = |r|^2, \tag{8}$$

where R denotes the intensity reflectivity.

For absorbing materials such as metals, the refractive index of the second medium becomes complex, $\tilde{n}_2 = n_2 + ik_2$. At normal incidence, the Fresnel reflection coefficient is obtained by replacing n_2 with $\tilde{n}_2$, yielding

$$R = \left| \frac{n_1 - \tilde{n}_2}{n_1 + \tilde{n}_2} \right|^2. \tag{9}$$

This expression describes the interface reflectivity only; absorption losses arise from field penetration and dissipation within the metallic layer and are fully captured in multilayer optical models discussed in Section 2.3.

In microcavities and distributed Bragg reflectors, light undergoes multiple reflections within a stack of thin films. The overall optical response cannot be described by a single interface, but instead results from interference between forward- and backward-propagating waves in each layer. This problem is conveniently treated using the TMM, which provides the complex reflection and transmission coefficients of a multilayer structure at a given wavelength and angle of incidence [41].

2.2.1 Transfer matrix formalism (TMM)

TMM is an invaluable tool for the design and characterisation of multilayer optical structures such as DBR–DBR microcavities. Derived from Maxwell's equations and the Fresnel coefficients, the method accounts for the multiple internal reflections that occur at each interface and the resulting constructive and destructive interference effects.

In this formalism, each layer is represented by a 2×2 matrix describing how electromagnetic waves propagate within it. The matrix depends on the complex refractive index of the material, its physical thickness, and the incidence angle and polarization of the incoming light. By multiplying the matrices of all layers in the order in which they appear in the stack, the overall transfer matrix of the multilayer system is obtained. From this, the reflected, transmitted, and absorbed intensities can be calculated as functions of wavelength and angle.

In addition to spectral properties, the TMM also allows the determination of the electric field distributions within the structure. Consequently, any planar cavity whether metal-clad, dielectric, or hybrid can be modeled to predict how it modifies the propagation, confinement, and enhancement of light.

2.3 Metal-clad microcavities

Metal mirrors are among the simplest and most widely used reflectors in optical microcavities due to their broad reflectivity across the visible spectrum and ease of fabrication. Common materials include silver (Ag), gold (Au), and aluminum (Al), each chosen for specific spectral and fabrication requirements. Their high reflectivity originates from the large difference between the real and imaginary parts of their complex refractive index,

$$\tilde{n} = n + ik, \tag{10}$$

where n is the refractive index and k is the extinction coefficient that accounts for absorption losses in the material. The reflectivity R at normal incidence can be expressed as

$$R = \left| \frac{\tilde{n} - 1}{\tilde{n} + 1} \right|^2 = \frac{(n-1)^2 + k^2}{(n+1)^2 + k^2}. \tag{11}$$

From this expression, it is evident that materials with large k (i.e., metals) can achieve high reflectivity, although this comes at the cost of increased absorption [40].

Figure 2 shows the calculated reflectivity spectra of Ag, Au, and Al mirrors, demonstrating their broadband optical response across the visible range. Among them, Ag exhibits the highest reflectivity and the lowest absorption losses, making it the preferred choice for visible-range optical cavities. The lower reflectivity of Au and Ag, particularly at shorter wavelengths, arises from their higher intrinsic absorption.

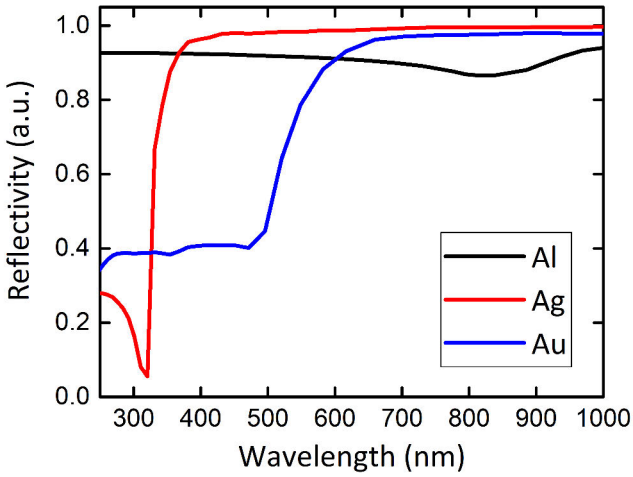

Figure 2. Reflectivity spectra of Al, Ag, and Au mirrors calculated using tabulated optical constants. Data for the refractive indices and extinction coefficients are taken from Refs. [44, 45]. Ag exhibits the highest reflectivity and lowest absorption losses in the visible region, while Au shows reduced reflectivity at shorter wavelengths due to increased interband absorption.

In practical microcavity design, one mirror (usually the bottom one) is made thick enough to be completely opaque, while the top mirror is made semi-transparent to allow light to couple in and out of the cavity. The reflectivity and transmission of these metal layers can be tailored by adjusting their thickness during deposition, typically using techniques such as thermal evaporation, e-beam evaporation, or sputtering.

An additional advantage of metal-clad microcavities is their compatibility with electrically driven device architectures. Because metals simultaneously serve as efficient reflectors and electrodes, they enable straightforward integration into structures such as OLEDs and polariton LEDs without requiring separate transparent conductive layers.

However, the major drawback of metallic mirrors is their significant absorption losses, which limit the achievable cavity quality factor (Q) to typically below 100. The Q-factor, which quantifies how long light is confined within the cavity, is inversely proportional to the total optical losses. In metal mirrors, these losses arise from both absorption within the metal and imperfect reflectivity. Consequently, the linewidth of the cavity mode broadens, reducing the field enhancement and hindering the observation of phenomena such as lasing.

Despite these limitations, metal-clad cavities remain valuable for proof-of-concept studies and for applications where broadband operation, simplicity, and electrical contact are prioritized over achieving ultrahigh Q-factors.

2.4 Distributed Bragg reflectors (DBRs)

An alternative to metallic mirrors in microcavity structures is the use of DBRs, which provide high optical confinement through distributed feedback. A DBR, as shown in Figure 3(a), consists of a periodic stack of alternating high- and low-refractive-index dielectric layers, each with an optical thickness of one quarter of the design wavelength ($\lambda_{\text{res}}/4n$). This multilayer arrangement produces constructive interference for the reflected waves and destructive interference for the transmitted ones, thereby creating a wavelength band of high reflectivity known as the photonic stopband (Figure 3(b)).

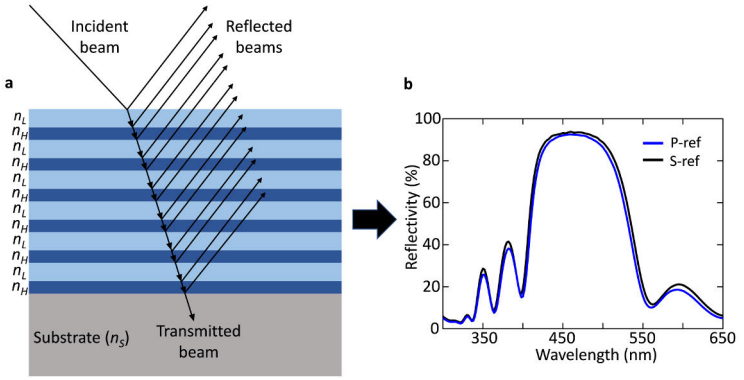

Figure 3. (a) Schematic diagram of a multilayer DBR, illustrating the constructive interference of reflected beams within alternating high- and low-index layers. (b) Experimental reflectivity of the six-pair TiOH/PVA–Nafion DBR reported in Publication II, displaying the characteristic stopband centered near the design wavelength. P- and S-polarized spectra show excellent agreement.

In planar microresonators, an optical cavity sandwiched between two highly reflective DBRs allows for strong vertical photon confinement. The reflectivity of a DBR stack depends primarily on two parameters: the refractive index contrast between the high (n_H) and low (n_L) index materials, and the number of layer pairs (N). Each pair contributes to the overall reflectivity through interference at each interface. The maximum reflectivity at normal incidence for a DBR is given by

$$R_{\text{max}} = \frac{\left(1 - \frac{n_C}{n_{\text{ext}}}\left(\frac{n_H}{n_L}\right)^{2N}\right)^2}{\left(1 + \frac{n_C}{n_{\text{ext}}}\left(\frac{n_H}{n_L}\right)^{2N}\right)^2}, \tag{12}$$

where n_C is the refractive index of the cavity medium, n_{ext} is that of the external medium, and N is the number of high/low index pairs in the stack. The stopband width $\Delta\lambda$, i.e., the range of wavelengths over which high reflectivity is maintained,

increases with the refractive index contrast $\Delta n = n_H - n_L$ according to

$$\frac{\Delta\lambda}{\lambda_{\mathrm{DBR}}} = \frac{4}{\pi}\sin^{-1}\left(\frac{n_H - n_L}{n_H + n_L}\right), \tag{13}$$

where λ_{DBR} is the central (Bragg) wavelength of the stopband. These relations follow the standard thin-film interference model.

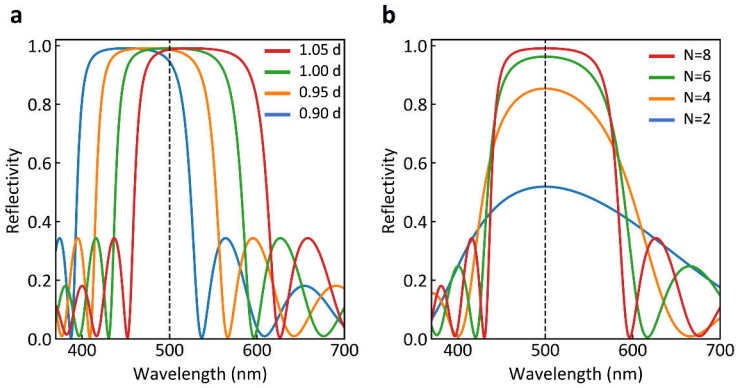

Figure 4. (a) Reflectivity simulation of a quarter-wave DBR as the optical thickness of each layer deviates from the ideal value $d = \lambda/4n$. Even small deviations shift the stopband and distort its symmetry. (b) Influence of the number of DBR pairs N on the reflectivity. Increasing N enhances the stopband reflectivity and narrows the passband regions.

Compared to metal mirrors, DBRs exhibit minimal absorption losses and higher optical quality factors (Q), often exceeding several thousand. This makes them essential components in VCSELs, high-Q resonators, and microcavity polariton structures. However, conventional DBRs are typically fabricated using vacuum-based deposition techniques. To demonstrate an alternative approach, we developed a fully solution-processed DBR (Figure 3b) and an empty microcavity comprising two six-pair mirrors separated by a 164 nm spacer layer, as shown in Figure 5 and described in Publication I. The resulting structure exhibits a distinct cavity mode centered at 510 nm with a quality factor of 91 and enables low-cost, scalable fabrication of dielectric mirrors under ambient conditions.

In this approach, alternating layers of a high-refractive-index titanium oxide hydrate/poly(vinyl alcohol) (TiOH/PVA) hybrid and a low-index Nafion polymer were sequentially deposited via automated dip-coating. This method provides nanometer-level control over film thickness and ensures excellent reproducibility across multiple deposition cycles. By carefully optimizing the deposition parameters, six-pair DBRs with reflectivity exceeding 80% were achieved, corresponding to quality factors among the highest reported for sub-10-pair solution-processed systems.

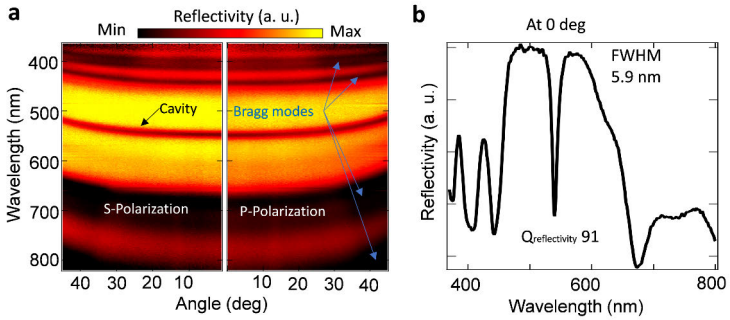

Figure 5. (a) Experimental angle-resolved reflectivity map of the empty microcavity formed by two six-pair DBRs and a 164 nm cavity spacer. The cavity mode and higher-order Bragg modes are visible for both s- and p-polarizations. (b) Normal-incidence reflectivity of the same structure, revealing a cavity-mode FWHM of 5.9 nm, corresponding to a cavity quality factor of $Q = 91$. Data reproduced from Publication I.

For comparison, conventional vacuum-deposited DBRs based on dielectric pairs such as SiO_2/TiO_2 or AlGaAs/AlAs typically achieve reflectivities exceeding 99% and support cavity quality factors ranging from several hundred to several thousand depending on cavity design and optical losses [25, 26]. Historically, most solution-processed DBRs exhibited reflectivities of ∼70–80%, limiting achievable cavity quality factors and hindering strong-coupling applications [27]. In this work, optimized polymer–inorganic multilayer DBRs fabricated entirely by solution processing achieve reflectivities approaching ∼95% and cavity quality factors up to ∼300, enabling robust strong light–matter coupling and polariton lasing in solution-processed microcavities [30]. These developments indicate that solution-processed DBRs can approach the optical performance of vacuum-deposited mirrors while offering advantages in cost, scalability, and ambient fabrication.

2.5 Solvents orthogonality and interlayer compatibility in solution-processed DBRs and microcavities

Solution-processed optical microcavities and DBRs are commonly fabricated using orthogonal solvent systems, where each layer is deposited from a solvent that does not dissolve or swell the underlying film. This approach is widely adopted to enable multilayer stacking without interfacial mixing. However, solvent orthogonality alone does not determine the optical quality or feasibility of multilayer microcavities.

In practice, the formation of high-quality DBRs requires a balance between interlayer stability, optical smoothness, and interfacial adhesion, rather than strict solvent orthogonality. In this thesis, high-reflectivity DBRs were realized using TiOH/PVA and Nafion layers, despite both materials being processed from polar solvents. The success of this system arises from the fact that, after deposition and drying, each layer

becomes effectively insoluble, enabling multilayer growth without re-dissolution.

The TiOH/PVA layers form hybrid organic–inorganic networks through hydrogen bonding and coordination between Ti–OH groups and PVA hydroxyls, leading to reduced polymer chain mobility and enhanced solvent resistance [46]. Similarly, Nafion films reorganize during drying into stable ionic domains, which makes them resistant to later solvent exposure. This stability allows sharp enough optical interfaces and smooth multilayer stacks to be maintained even without strictly orthogonal solvents [47].

Importantly, a moderate degree of chemical compatibility between adjacent layers can be advantageous for the fabrication of solution-processed optical microcavities. Partial interfacial interactions improve adhesion and suppress dewetting, which is essential for maintaining smooth and uniform films over many deposition cycles. In contrast, excessively orthogonal material–solvent combinations can hinder wetting and prevent the formation of continuous layers. For example, replacing Nafion with a fluorinated polymer processed from a perfluorinated solvent led to severe dewetting of subsequently deposited TiOH/PVA layers, demonstrating that extreme solvent orthogonality is not suitable for solution-processed DBR fabrication.

These considerations demonstrate that the key requirement for solution-processed optical microcavities is not strict solvent orthogonality, but the formation of stabilized layers that resist re-dissolution while maintaining sufficient interfacial compatibility. Identifying this balance is central to the fabrication of organic and hybrid microcavities.

In this chapter, the fundamental concepts related to optical microcavities have been introduced, beginning with the principles of photon confinement and resonance in planar Fabry–Pérot geometries, including their angular dispersion and quality-factor limitations. Both metal-clad and dielectric cavity structures were discussed, highlighting their respective advantages and limitations in terms of fabrication simplicity, optical losses, and achievable quality factors. While metallic mirrors offer broadband reflectivity and electrical conductivity, their high absorption restricts the attainable Q values. In contrast, dielectric DBRs provide superior optical confinement through constructive interference within multilayer stacks, enabling narrow linewidths and high reflectivity essential for studying light–matter interactions.

To address the cost, scalability, and material-compatibility challenges associated with vacuum-deposited DBRs, a fully solution-processed TiOH/PVA–Nafion reflector system was developed. These dielectric mirrors combine high refractive-index contrast with mechanical robustness and ambient-condition processing, enabling the fabrication of all-solution-processed microcavities. The resulting structures exhibit distinct cavity modes and quality factors among the highest reported for comparable low-pair-count solution-processed DBR systems, demonstrating that high optical performance can be achieved using low-cost fabrication routes.

Finally, the role of solvent orthogonality and interlayer compatibility in solution-processed multilayer optics was examined, emphasizing that stabilized layer formation and controlled interfacial interactions are more critical than strict solvent orthogonality.

Together, the concepts, modelling tools, and materials introduced in this chapter establish the physical and technological foundation for the subsequent chapters, where these microcavities are employed to investigate strong light–matter coupling, polariton lasing, and their application in optoelectronic devices.

---

3 Organic polaritons

Note: This chapter introduces the theoretical framework of strong light–matter coupling and summarizes the experimental observations reported in Publications II and III, where strong coupling and polariton formation were demonstrated in solution-processed microcavities.
Unless otherwise stated, the theoretical background and equations discussed in this chapter are based on standard formulations found in Refs. [48].

The solution-processed microcavities developed in the previous chapter provide an excellent optical platform for exploring light–matter interactions under confinement. By introducing an active organic material into these structures, it becomes possible to reach the strong light–matter coupling, where the exchange of energy between excitons and cavity photons occurs faster than their respective decay rates [1]. In this regime, the system gives rise to new hybrid light–matter quasiparticles known as exciton–polaritons. These states inherit properties from both photons and excitons, combining long-range coherence and delocalization with strong nonlinear interactions. These can be harnessed to control optical emission, energy transfer, and lasing processes at room temperature. This chapter focuses on the realization, optical characterization, and analysis of fully solution-processed organic microcavities that support strong light–matter coupling, establishing a scalable route toward low-cost polaritonic devices [43].

3.1 Organic semiconductors and frenkel excitons

Organic semiconductors are carbon-based materials that exhibit semiconducting behavior due to the delocalization of π-electrons along conjugated molecular backbones [49]. They are typically composed of carbon and hydrogen, with oxygen, nitrogen, or sulfur atoms often incorporated to tailor the properties. They have emerged as a versatile class of materials for optoelectronic applications, including solar cells, transistors, light-emitting diodes, and lasers. Their key advantages over conventional inorganic semiconductors are that they are lightweight, mechanically flexible, and compatible with large-area, low-temperature, and cost-effective solution-processing techniques. Moreover, their electronic and optical properties can be tailored and tuned through chemical synthesis. By modifying molecular structures or incorporating specific functional groups, one can control properties such as absorption, emis-

sion, photostability, and charge-transport characteristics. This has led to rapid advances in organic light-emitting diodes (OLEDs) and related technologies, where emission can be engineered across the entire visible spectrum [50].

In contrast to crystalline inorganic semiconductors, where energy bands originate from extended atomic orbitals, organic materials are composed of discrete molecules held together by weak van der Waals interactions [50]. The electronic states of such molecular solids are therefore largely localized on individual molecules. Optical absorption and emission arise from transitions between the highest occupied molecular orbital (HOMO) and the lowest unoccupied molecular orbital (LUMO), analogous to the valence and conduction bands in inorganic systems. In conjugated molecules, the alternating single and double carbon–carbon bonds create a delocalized π-electron system, which lowers the energy gap into the visible region and enables efficient interaction with light.

When a photon is absorbed, an electron is promoted from the HOMO to the LUMO, leaving behind a positively charged hole. The Coulombic attraction between these oppositely charged particles forms a bound electron–hole pair known as an exciton. The nature of this exciton depends strongly on the dielectric environment and the degree of electronic delocalization. Inorganic semiconductors with high dielectric constants form weakly bound Wannier–Mott excitons, which are delocalized over many lattice sites and possess binding energies on the order of 10 meV. Such excitons are easily dissociated at room temperature. Organic semiconductors, on the other hand, exhibit strongly localized Frenkel excitons with binding energies typically around 0.5–1 eV [49, 50]. These excitons are confined to individual molecules and remain stable even at room temperature, making them ideal for exploring strong light–matter coupling phenomena without the need for cryogenic operation.

Exciton dissociation in organic semiconductors can occur radiatively or non-radiatively. The fraction of radiative decays over non-radiative decays defines the photoluminescence quantum yield (PLQY)It is expressed as

$$\mathrm{PLQY} = \frac{k_{\mathrm{r}}}{k_{\mathrm{r}} + k_{\mathrm{nr}}}, \tag{14}$$

where k_{r} and k_{nr} are the radiative and non-radiative decay rates, respectively. Upon excitation, electron–hole pairs can form either singlet or triplet excitons depending on the relative spin orientation of the two charge carriers. Optical excitation obeys spin selection rules ($\Delta S = 0$), so population is initially created in singlet excited states (S_1) [50]. However, triplet excitons can also form indirectly through intersystem crossing (ISC), a non-radiative process in which an excited singlet state converts into a triplet state with a characteristic rate k_{ISC}. The fraction of excitations that undergo ISC is

$$\Phi_T = \frac{k_{\mathrm{ISC}}}{k_r + k_{nr} + k_{\mathrm{ISC}}}, \tag{15}$$

or via singlet fission in systems where $E(S_1) \gtrsim 2E(T_1)$ [49]. In materials with strong spin-orbit coupling (such as those containing heavy metal atoms) or under two–photon excitation, direct population of triplet states may also occur. In contrast, electrical excitation generates electron–hole pairs with random spin orientations, leading to the formation of singlet and triplet excitons in 1:3 ratio prior to any spin mixing [51].

To overcome these spin-related losses and achieve efficient light emission, several classes of emissive organic materials have been developed. Phosphorescent organometallic complexes exploit strong spin–orbit coupling from heavy-metal atoms (such as iridium or platinum) to enable radiative decay from triplet states [51]. Alternatively, thermally activated delayed fluorescence (TADF) materials utilize small singlet–triplet energy gaps (ΔE_{ST}) to promote reverse intersystem crossing (RISC), converting non-emissive triplet excitons back into radiative singlets [52]. Both approaches significantly enhance internal quantum efficiency, enabling near-unity emission yields and making them particularly attractive for high-performance organic light-emitting diodes.

The organic emitters used in this chapter, along with their photophysical properties and preparation methods, are described in Chapter 6. Here, we focus on how these materials behave when embedded in microcavities and subjected to strong light–matter coupling.

3.2 Fundamental light–matter interaction

When light propagates through a medium, its behaviour differs markedly from that in vacuum. In free space, photons are quanta of the electromagnetic field with angular frequency $\omega = 2\pi\nu$, energy $E = \hbar\omega = h\nu$, and momentum $\mathbf{k} = (2\pi/\lambda)\hat{\mathbf{k}}$, where λ is the wavelength in vacuum and $\hat{\mathbf{k}}$ defines the propagation direction. The dispersion relation of photons in vacuum follows a linear form,

$$\omega(\mathbf{k}) = c|\mathbf{k}|, \tag{16}$$

where c is the speed of light. In contrast, when light enters a dielectric medium, its propagation is influenced by the polarization response of matter, which modifies the dispersion to

$$\mathbf{k} = \tilde{n}(\omega)\mathbf{k}_{\mathrm{vac}}, \tag{17}$$

where $\tilde{n}(\omega)$ is the complex refractive index of the medium. Far from material resonances, this simple refractive description suffices. However, near resonant frequencies, the electromagnetic field and the medium's electronic excitations interact more intricately, giving rise to new collective states of light and matter.

3.2.1 Weak coupling regime and the Purcell effect

In the weak coupling regime, the interaction strength g between light and matter is much smaller than both the cavity photon decay rate κ and the emitter dephasing rate γ,

$$g \ll (\kappa, \gamma). \tag{18}$$

Under these conditions, the exchange of energy between the emitter and the cavity field is irreversible, and no coherent light–matter hybridisation occurs. Instead, the cavity modifies the electromagnetic environment experienced by the emitter by changing the local density of optical states (LDOS) [53].

When the emitter's optical transition is resonant with a cavity mode, this modified LDOS can enhance the spontaneous emission rate into that mode. The maximum enhancement is described by the Purcell factor,

$$F_{\mathrm{P}} = \frac{3}{4\pi^2} \left(\frac{\lambda_c}{n_{\mathrm{eff}}} \right)^3 \frac{Q}{V_{\mathrm{eff}}}, \tag{19}$$

where λ_c is the cavity resonant wavelength, n_{eff} is the effective refractive index, Q is the cavity quality factor, and V_{eff} is the effective mode volume [54].

A high Q (low optical loss) and a small V_{eff} (tight confinement) therefore increase the rate at which an excited emitter radiatively decays through the cavity mode. This enhancement of spontaneous emission characterises the weak coupling regime, where the emitter and the cavity mode do not form hybridised states and behave as independent excitonic and photonic modes.

3.2.2 Strong coupling regime

When the interaction strength between light and matter becomes comparable to or greater than their respective loss rates, the system enters the strong coupling regime. In this regime, energy is exchanged coherently and reversibly between the confined optical mode of the cavity and the electronic excitation of the active material. As a result, the photon and exciton modes hybridize to form new eigenstates known as exciton-polaritons, which are part light and part matter quasiparticles.

The behaviour of such a system can be understood intuitively using a classical analogy of two coupled harmonic oscillators. Consider two identical masses, each attached to a spring, and connected by a weak coupling spring. When the coupling is absent, the two oscillators move independently at the same natural frequency. Once coupled, their individual resonances split into two new normal modes, one where the masses move in phase and another where they move out of phase. The frequency separation between these modes increases with the coupling strength. This frequency splitting is the classical analogue of the Rabi splitting observed in optical micro-

cavities, where the electromagnetic field (photon mode) and the material excitation (exciton mode) exchange energy coherently [55].

The strong coupling is determined by the condition

$$g > \frac{1}{2}\sqrt{\gamma^2 + \kappa^2}, \tag{20}$$

where g is the coupling strength, γ is the exciton dephasing rate, and κ is the photon decay rate. The coupling strength depends on the transition dipole moment μ, the cavity mode volume V_{eff}, and the number of coherently coupled dipoles N, such that

$$g = \mu\sqrt{\frac{N\hbar\omega_{\text{c}}}{2\varepsilon_0 V_{\text{eff}}}}. \tag{21}$$

From a quantum electrodynamical perspective, the strong coupling regime is described by the Jaynes–Cummings model, which treats the interaction between a two-level emitter and a single mode of the quantized electromagnetic field. The system Hamiltonian is expressed as

$$\hat{H}_{\text{JC}} = \hbar\omega_{\text{c}}\hat{a}^\dagger\hat{a} + \frac{1}{2}\hbar\omega_{\text{x}}\hat{\sigma}_z + \hbar g\left(\hat{a}^\dagger\hat{\sigma}_- + \hat{a}\hat{\sigma}_+\right), \tag{22}$$

where $\hat{a}^\dagger$ and $\hat{a}$ are the photon creation and annihilation operators, $\hat{\sigma}_z$ is the Pauli operator describing the two-level system with transition frequency ω_{x}, and $\hat{\sigma}_\pm$ are the raising and lowering operators for the emitter [14].

Diagonalizing this Hamiltonian yields two hybrid eigenstates, the upper ($|P_+\rangle$) and lower ($|P_-\rangle$) polariton states:

$$|P_\pm\rangle = \alpha_\pm|e,0\rangle \pm \beta_\pm|g,1\rangle, \tag{23}$$

where $|e,0\rangle$ and $|g,1\rangle$ represent the uncoupled exciton and photon states, respectively. The coefficients $\alpha_\pm$ and $\beta_\pm$, known as the Hopfield coefficients, quantify the excitonic and photonic character of each polariton branch [56]. Far below resonance, the lower polariton (LP) branch is predominantly excitonic in nature, while the upper polariton (UP) branch is mainly photonic. Conversely, far above resonance, the LPB becomes photonic and the UPB excitonic. At exact resonance, the two modes are equally mixed, containing 50% exciton and 50% photon character. This composition determines the effective mass, group velocity, and nonlinear interaction strength of polaritons and is therefore crucial for understanding their optical and dynamical properties.

At resonance ($\omega_{\text{c}} = \omega_{\text{x}}$), the two polariton branches are split by an energy

$$\hbar\Omega_{\text{R}} = 2\hbar g, \tag{24}$$

where Ω_{R} is the Rabi frequency, representing the rate of coherent energy exchange between light and matter. Experimentally, this appears as an anticrossing in the

angle-resolved dispersion relation, separating the upper (UPB) and lower (LPB) polariton branches.

In organic systems, strong coupling is facilitated by the large oscillator strength and strong dipole moments of Frenkel excitons. These properties enable strong coupling and polariton formation at room temperature.

3.2.3 Criteria for strong light–matter coupling

Having introduced the physical origin of polariton formation, it is useful to state the conditions under which a system is considered to be in the strong coupling regime. Strong coupling arises when the rate of coherent energy exchange between the molecular transition and the cavity mode exceeds the relevant dissipation channels. In other words, the interaction strength must dominate over both the exciton dephasing rate γ and the cavity photon decay rate κ.

A commonly used criterion is

$$2g > \gamma + \kappa, \tag{25}$$

which expresses that the coherent coupling must outpace the average losses of the two subsystems. A more stringent formulation requires that the coupling individually overcomes each loss channel,

$$2g > \gamma \qquad \text{and} \qquad 2g > \kappa, \tag{26}$$

ensuring that neither excitonic nor photonic dissipation quenches the coherent exchange of energy.

Experimentally, strong coupling is identified from an anticrossing in the angle-resolved reflectivity dispersion, from which the Rabi splitting is obtained. For the splitting to be spectroscopically observable, it must exceed the linewidths of the uncoupled exciton and cavity modes. This requirement is often written as

$$\hbar\Omega_{\mathrm{R}} > \frac{\Gamma_{\mathrm{x}} + \Gamma_{\mathrm{c}}}{2}, \tag{27}$$

where Γ_{x} and Γ_{c} denote the full width at half maximum (FWHM) of the excitonic absorption and cavity mode, respectively. When this condition is met, the upper and LP branches appear as two distinct, spectrally separated features rather than a single broadened resonance.

Together, these criteria ensure that the observed mode splitting reflects genuine hybridisation of light and matter, rather than an artefact of absorption, broadening, or perturbative cavity effects.

3.2.4 Coupled harmonic oscillator model (CHOM)

The interaction between cavity photons and excitons can be described conceptually using the CHOM. In this classical picture, the exciton and photon behave as two oscillators with natural frequencies ω_{x} and ω_{c} that are coupled with strength g. The resulting hybridization gives rise to two new normal modes that are analogous to the lower and upper polariton branches observed in strongly coupled systems.

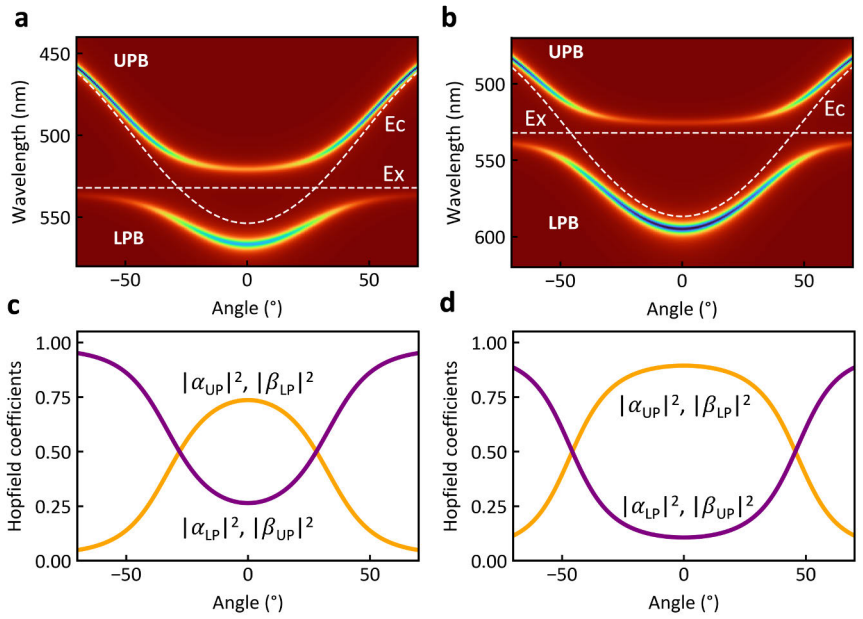

Figure 6. (a,b) Simulated angle-resolved reflectivity maps for two different cavity detunings, showing the characteristic *anticrossing* behaviour that evidences the onset of strong light–matter coupling. The dashed lines indicate the uncoupled cavity and exciton modes, while the solid curves represent the hybrid UP and LP branches obtained from the CHOM. (c,d) Corresponding Hopfield coefficients, illustrating the evolution of the photonic ($|\beta|^2$) and excitonic ($|\alpha|^2$) fractions of the LP branch as a function of angle. At resonance, both components contribute equally, confirming the mixed light–matter nature of exciton-polaritons.

Mathematically, the system can be represented by the following matrix form:

$$\begin{pmatrix} E_{\mathrm{c}}(k) & g \\ g & E_{\mathrm{x}}(k) \end{pmatrix}, \tag{28}$$

where $E_{\mathrm{c}}(k)$ is the cavity photon dispersion, $E_{\mathrm{x}}(k)$ is the exciton energy (assumed nearly flat due to the large exciton mass), and g is the coupling strength between the two oscillators.

Solving the eigenvalue problem yields two new energy branches:

$$E_{\pm}(k) = \frac{E_{\mathrm{c}}(k) + E_{\mathrm{x}}(k)}{2} \pm \frac{1}{2}\sqrt{(E_{\mathrm{c}}(k) - E_{\mathrm{x}}(k))^2 + 4g^2}. \tag{29}$$

These correspond to the upper (E_+) and lower (E_-) polariton branches, respectively. At the resonance condition $E_c = E_x$, the energy splitting between the two modes is given by

$$\hbar\Omega_R = 2g, \tag{30}$$

where Ω_R is the Rabi frequency. The magnitude of this splitting is a direct measure of the strength of the light–matter interaction and defines the onset of the strong coupling regime.

Experimentally, this anti-crossing behaviour appears as a distinct splitting in the angle-resolved reflectivity or photoluminescence dispersion, confirming the formation of hybrid light–matter states. This behaviour can be visualized through numerical simulations based on the CHOM, as shown in Figure 6. The CHOM therefore provides an intuitive link between the classical and quantum mechanical descriptions of polariton formation and serves as the foundation for understanding polariton condensation and lasing phenomena discussed in the following sections.

3.2.5 Relaxation mechanisms in organic polariton microcavities

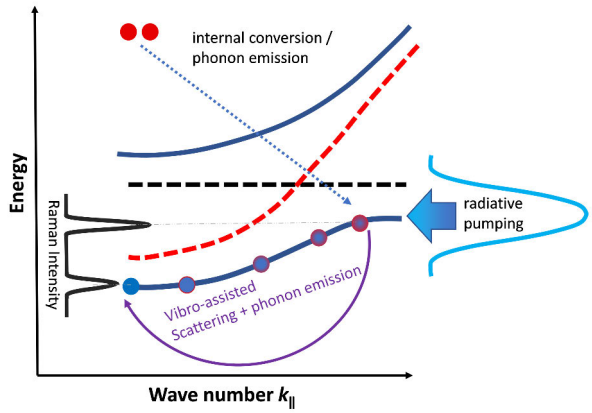

Figure 7. Schematic illustration of relaxation pathways in organic microcavities. Strong exciton–phonon coupling enables efficient vibron-assisted scattering and phonon emission into the LP branch, facilitating relaxation toward low-momentum states. In addition, radiative pumping from weakly coupled exciton states can contribute to the population of lower-energy polariton modes. The diagram summarizes the relaxation channels relevant for organic microcavity systems.

In organic microcavities, where exciton–phonon coupling is strong, relaxation dynamics are governed by different mechanisms compared to inorganic systems. Vibron-assisted scattering mediated by intramolecular vibrations provides an efficient channel for energy relaxation into the LP branch. Additional mechanisms, such as radiative pumping by weakly coupled exciton states, can also contribute to the population of low-energy polariton states [57–59].

The relaxation pathways relevant for organic microcavities are illustrated schematically in Figure 7, highlighting phonon-mediated scattering, vibronic channels, and radiative pumping processes that populate the LP branch.

3.2.6 Other Types of polaritons

While the experimental work presented in this thesis focuses on exciton–polaritons, it is instructive to briefly discuss other classes of light–matter quasiparticles that share conceptual similarities. These include surface plasmon polaritons (SPPs), plexcitons, and phonon–polaritons, each arising from the coupling of photons with different collective excitations in matter.

In metals, collective oscillations of conduction electrons known as plasmons can couple to electromagnetic waves at a metal–dielectric interface, forming surface plasmon polaritons (SPPs) [60]. The resulting electromagnetic field is confined near the interface and decays exponentially into both media, enabling the confinement and guiding of light at subwavelength scales, far below the diffraction limit. This intense field localization makes SPPs highly sensitive to changes in the surrounding environment, leading to their use in nanoscale optical sensing, photonic circuitry, and surface-enhanced spectroscopy.

When plasmons couple strongly to excitons in nearby molecules or semiconductors, the resulting hybrid quasiparticles are known as plexcitons [61]. These states inherit properties from both constituents, the field confinement and sensitivity of plasmons, and the resonant optical response of excitons, allowing enhanced spontaneous emission, long-range energy transfer, and potential applications in efficient light-harvesting, photocatalysis, and nanophotonic switching.

A further example is the phonon–polariton, which emerges from the coupling of infrared photons with optical phonons that are the quantized vibrational modes of a crystal lattice. The resulting hybrid modes exhibit strong field confinement and tunability in the mid-infrared spectral region, enabling near-field heat management, thermal emission engineering, and sub-diffraction imaging [62].

Although the following chapters focus on exciton–polaritons in organic microcavities, the broader landscape of polaritonic systems illustrates the universality of strong light–matter coupling and its growing relevance across photonics, nanotechnology, and materials science.

3.3 Demonstration of strong light–matter Coupling in organic microcavities

Building on the high optical quality of the solution-processed dielectric microcavities introduced earlier in this thesis, Publications I–IV establish strong exciton–photon coupling in a range of organic emitters using scalable fabrication routes. Strong cou-

pling is identified through clear avoided crossings between cavity photon modes and molecular excitons in angle-resolved reflectivity, together with quantitative agreement with CHOM. These studies demonstrate that solution-processed architectures can achieve coupling strengths comparable to those obtained in vacuum-deposited microcavities.

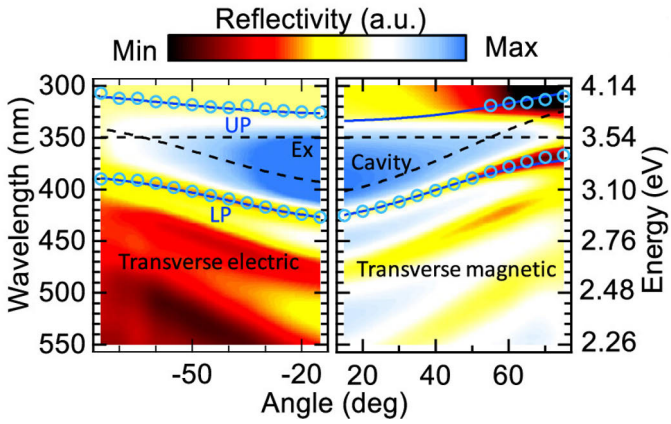

Figure 8. Angle-resolved reflectivity spectra of the microcavity for transverse electric (left) and transverse magnetic (right) polarization adapted form Publication I. The observed anticrossing between the exciton resonance and the cavity photon mode demonstrates the onset of strong light–matter coupling. Open circles show the experimentally extracted dispersions, while the dashed curves represent the uncoupled exciton and cavity modes used in the CHOM.

In Publication I, strong coupling was demonstrated in a hybrid microcavity consisting of a solution-processed dielectric DBR and a thermally evaporated metal top mirror embedding a neat film of the fluorescent emitter TDAF. Angle-resolved reflectivity measurements for both transverse-electric and transverse-magnetic polarizations reveal pronounced anticrossings between the cavity mode and the TDAF exciton (Figure 8), providing clear evidence of the formation of UP and LP branches. CHO fits yield vacuum Rabi splittings of approximately 750–800 meV, well exceeding the combined exciton and cavity linewidths.

Publication II extended this approach to fully solution-processed planar microcavities incorporating Rhodamine 6G dispersed in a PVA matrix. Rhodamine 6G is an organic dye with a large oscillator strength and a broad excitonic resonance at room temperature. By varying the dye concentration while keeping the cavity geometry fixed, the exciton–photon coupling strength was tuned over a wide range. Angle-resolved reflectivity measurements show upper and LP branches within the DBR stopband for all concentrations studied (Figure 9). Coupled-oscillator fits yield Rabi splittings increasing from approximately 130 meV to over 400 meV with increasing concentration, reflecting the increase in collective oscillator strength. Comparison with silver-clad and sputtered-DBR reference cavities shows that the solution-

processed DBR microcavities achieve similar coupling strengths, while avoiding the material degradation observed during sputtering.

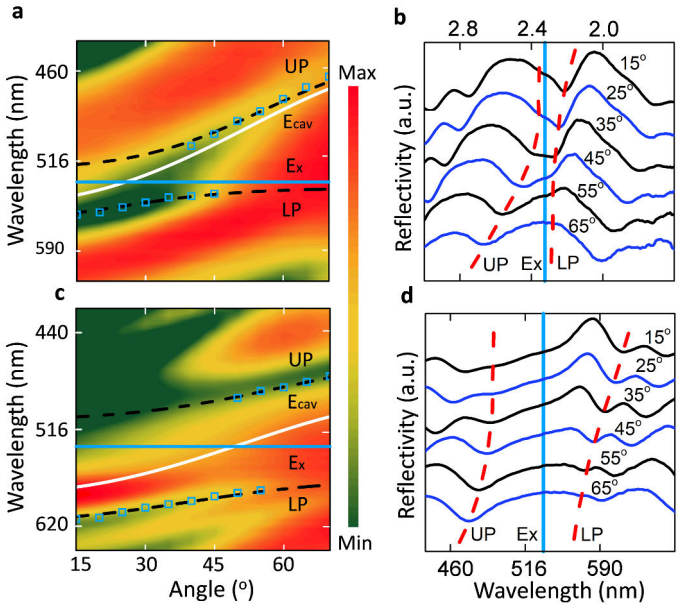

Figure 9. Angle-resolved reflectivity spectra of the microcavity for two cavity detunings adapted from Publication 2. (a,c) Reflectivity maps showing the hybridization of the cavity photon mode E_{cav} with the exciton resonance E_{x}, resulting in the lower (LP) and upper (UP) polariton branches. The dashed lines represent CHOM fits to the data, and the square points mark the experimentally extracted peak positions. (b,d) Reflectivity spectra at selected angles, highlighting the anticrossing behaviour and the angular evolution of the polariton branches.

In DPAVB-based microcavities, strong exciton-photon coupling is evidenced by the appearance of clear avoided crossings in angle-resolved reflectivity. As shown in Figures 10(a,b), the cavity photon mode hybridizes with three distinct excitonic resonances of DPAVB (Ex_1, Ex_2, and Ex_3), resulting in the formation of four dispersive polaritonic branches: the UP, two middle polariton branches (MP_1 and MP_2), and the LP.

CHOM of the measured dispersions reproduces the experimental reflectivity maps and yields Rabi splittings of approximately 230 meV, 160 meV, and 130 meV for the respective light–matter interactions, in agreement with previously reported values for DPAVB-based microcavities. The observation of multiple well-resolved polariton branches and their characteristic anticrossing behaviour provides clear experimental evidence of strong light–matter hybridization in these fully solution-processed microcavities.

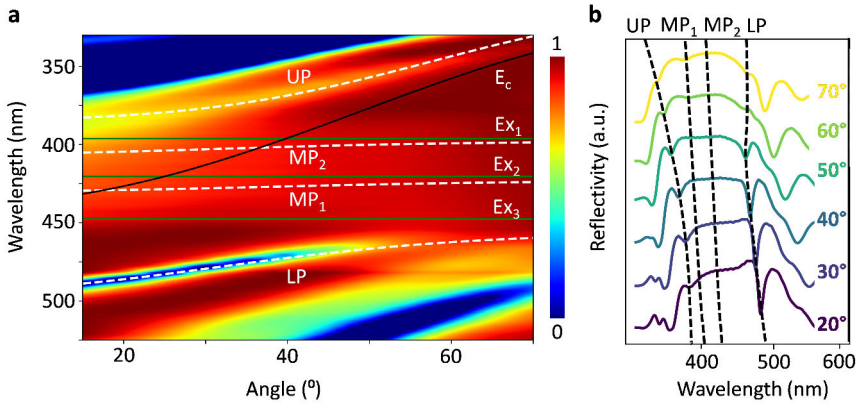

Figure 10. a) Angle-resolved reflectivity map of the DPAVB microcavity adapted from Publication III showing the formation of upper (UP), middle (MP_1, MP_2), and lower (LP) polariton branches resulting from strong coupling between the cavity mode E_c and multiple excitonic resonances $E_{x,1}$ and $E_{x,2}$. The dashed lines correspond to CHOM fits and the solid lines corresponds to a cavity mode and exciton resonences. (b) Reflectivity spectra at selected detection angles confirming the anticrossing behaviour and the evolution of the UP, MP, and LP branches with angle.

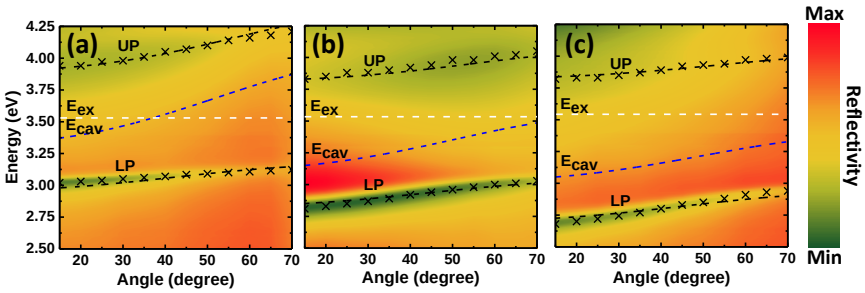

Figure 11. Angle-resolved reflectivity maps of the TDAF microcavity for three cavity detunings adapted from Publication IV. The coupling between the cavity photon mode E_{cav} and the TDAF exciton resonance E_{ex} leads to the formation of UP and LP polariton branches, as evidenced by the clear anticrossing behaviour. The dashed lines correspond to the uncoupled exciton and cavity dispersions, and the crosses indicate the experimentally extracted reflectivity minima used for CHOM analysis.

Publication IV employed strong coupling as a controlled platform to investigate electroluminescence dynamics in an operational OLED rather than to demonstrate new polaritonic eigenstates. Polaritonic OLEDs (POLEDs) based on neat TDAF films were fabricated in bottom-emitting microcavity architectures, with the LP energy systematically tuned to 2.95, 2.83, and 2.67 eV by varying the cavity thickness. Angle-resolved reflectivity measurements reveal clear anticrossings for all devices (Figure 11), and CHO fits yield Rabi splittings of 0.92, 0.88, and 0.96 eV for POLED 1–3, respectively, in agreement with previous reports on TDAF under strong coupling. Notably, even for the most negatively detuned device, where the LP lies at

2.67 eV, the LP retains a substantial excitonic fraction of approximately 28%, confirming that strong coupling persists despite deep negative detuning. Taken together, Publications I–IV demonstrate that strong light–matter coupling can be achieved reproducibly in organic microcavities fabricated using solution-based methods and integrated device architectures. While strong coupling enables access to polaritonic dispersion, high excitonic fractions, and nonlinear emission regimes, its impact on intramolecular excited-state dynamics remains strongly system dependent and is not necessarily manifested in delayed emission pathways. The results presented here provide the experimental basis for the polariton lasing studies discussed in the following section, while also defining the practical limits of cavity-induced effects on triplet-related processes in conventional fluorescent OLEDs.

In this chapter, the fundamental concepts and experimental realization of strong light–matter coupling in organic microcavities were presented. Starting from the theoretical description of exciton–photon hybridization, the transition from the weak to the strong coupling regime was discussed in terms of coherent energy exchange between the cavity mode and the molecular exciton. The coupled oscillator framework was introduced to describe the formation of the UP and LP branches, and the appearance of a resolvable Rabi splitting was identified as the experimental signature of strong coupling. Importantly, strong coupling is confirmed when the Rabi splitting exceeds the combined linewidths of the uncoupled exciton and cavity modes, ensuring that the two polariton branches can be distinguished spectrally.

A range of microcavity architectures—including metal-clad, hybrid metal–DBR, and fully solution-processed systems—were shown to satisfy this criterion using different organic emitters. The extracted Rabi splittings, extending from 170 meV to beyond 900 meV, demonstrate that solution-processed microcavities can achieve coupling strengths comparable to conventional vacuum-deposited devices. These findings establish a solid experimental basis for the following chapters, where the focus shifts from static strong coupling to dynamic phenomena such as polariton lasing and coherent light emission.

---

4 Organic polariton lasing

Note: This chapter presents the results reported in Publication III, focusing on polariton lasing in solution-processed microcavities.
Unless otherwise stated, the theoretical background and equations discussed in this chapter are based on standard formulations found in Refs. [48].

The achievement of strong light–matter coupling in solution-processed microcavities, as discussed in the previous chapter, provides the foundation for realizing coherent light emission through polariton lasing. Unlike conventional photon lasing, which requires population inversion and stimulated emission, polariton lasing arises from bosonic final-state stimulation, where exciton–polaritons undergo stimulated scattering into the lowest-energy states of the LP branch. This nonlinear process enables coherent light generation at significantly lower thresholds than photon lasing and can occur at room temperature [63–65].

In this chapter, we demonstrate that entirely solution-processed organic microcavities consisting of polymeric distributed Bragg reflectors and spin-coated active layers that can sustain strong coupling and reach the nonlinear regime characteristic of polariton lasing [30].

4.1 Photon lasing

Conventional photon lasing relies on three fundamental light–matter processes: absorption, spontaneous emission, and stimulated emission. When a photon with energy matching the electronic transition between two levels ($E_2 - E_1 = h\nu$) is absorbed, an electron is excited from the lower level to the higher one. This excited electron can subsequently relax back to the ground state by emitting a photon. In spontaneous emission, the photon is emitted randomly in phase and direction, whereas in stimulated emission, an incident photon induces the emission of a second photon that is coherent—identical in energy, phase, and propagation direction to the first. This process assists the amplification of light in a laser medium.

To achieve sustained amplification, the rate of stimulated emission must exceed that of absorption. This condition requires a population inversion, where the number of electrons in the excited state exceeds that in the ground state ($N_2 > N_1$). In thermal equilibrium, this situation does not naturally occur and must be achieved by optical or electrical pumping. Once population inversion is established, photons gen-

erated by stimulated emission are trapped between two mirrors forming a resonant cavity. One of the mirrors is made partially transmissive, allowing a fraction of the coherent light to escape as the laser output. Lasing begins when the gain provided by stimulated emission compensates for all optical losses within the cavity, a condition known as the lasing threshold.

The key signatures of photon lasing are a distinct threshold in the emission intensity, spectral narrowing due to coherence buildup, and the selection of a single cavity mode determined by the cavity length. Photon lasing therefore represents a regime in which coherence arises through population inversion and stimulated emission within a resonant optical cavity [41].

4.2 Photon vs. polariton lasing

While photon lasing relies on stimulated emission and inversion, polariton lasing emerges in the strong light–matter coupling regime, where excitons and photons hybridize into mixed quasiparticles, exciton–polaritons. These polaritons are bosons that can accumulate in the lowest energy state via stimulated scattering, even without population inversion [22, 26, 64, 65].

The key differences between photon and polariton lasing are summarized in Table 1.

Table 1. Comparison between photon lasing and polariton lasing.

Property	Photon Lasing	Polariton Lasing
Gain mechanism	Stimulated emission requiring population inversion	Stimulated scattering into a macroscopically occupied polariton state (no inversion)
Active species	Photons from electron–hole recombination	Exciton–polaritons (hybrid light–matter quasiparticles)
Coupling regime	Weak exciton–photon coupling	Strong exciton–photon coupling
Threshold condition	Population inversion ($N_2 > N_1$)	Final-state stimulation above a critical polariton density
Emission coherence	Coherence established by cavity feedback	Coherence from macroscopic occupation of a single polariton state
Spectral behavior	Single lasing mode; no anticrossing	Rabi-split polariton branches; lasing from the LP branch
Linewidth evolution	Abrupt narrowing at threshold	Progressive narrowing associated with condensation
Threshold power	High (inversion required)	Low (bosonic stimulation; no inversion)
Operation temperature	Limited by gain medium	Often room-temperature in organic systems
Emission origin	Electronic transitions	Emission from a polariton condensate on the LPB

4.3 Polariton lasing

In the previous section, conventional photon lasing was described as a process requiring population inversion and stimulated emission within an optical resonator. In contrast, polariton lasing arises from a fundamentally different mechanism that does not rely on population inversion. Instead, it is based on the macroscopic occupation of a single quantum state by exciton–polaritons [65, 66].

4.3.1 Polariton condensation

Exciton-polaritons possess small effective mass, typically on the order of $10^{-4}\, m_e$ near zero in-plane momentum, owing to their strong photonic component. This exceptionally low mass enables polaritons to reach quantum degeneracy and undergo condensation at temperatures far above those required for atomic Bose-Einstein condensates, which normally require cryogenic cooling [63, 64]. The LP inherits its dispersion primarily from the photonic component. To a good approximation, its effective mass scales inversely with the photonic fraction:

$$m_{\mathrm{LP}} \approx \frac{m_{\mathrm{ph}}}{|C_{\mathrm{ph}}|^2}, \tag{31}$$

where m_{ph} is the cavity photon effective mass and $|C_{\mathrm{ph}}|^2$ is the photonic Hopfield coefficient.

In organic semiconductors, the large exciton binding energy and strong oscillator strength of Frenkel excitons further facilitate polariton condensation at or near room temperature [22, 26, 58].

Following non-resonant optical excitation, polaritons are initially created at high energies on the LP. Through interactions with phonons and the exciton reservoir, they redistribute toward lower-energy states near $k \approx 0$. This relaxation is not a true thermalisation process as typically required for Bose–Einstein condensation, but is instead driven by stimulated scattering (bosonic final-state stimulation), which preferentially populates the lowest polariton states at sufficiently high excitation densities.

As the pump power increases, the polariton density rises. When the average interparticle distance becomes comparable to the polariton de Broglie wavelength,

$$\lambda_{\mathrm{dB}} = \frac{h}{\sqrt{2\pi m_{\mathrm{pol}} k_{\mathrm{B}} T}}, \tag{32}$$

the system approaches the critical density for condensation, given approximately by

$$n_c \lambda_{\mathrm{dB}}^2 \approx 1. \tag{33}$$

At this point, the polariton wavefunctions overlap significantly, and quantum statistics begin to dominate their behavior. Bosonic final-state stimulation enhances scattering into the already occupied lowest-energy state that leads to a rapid build-up

of population at $k \approx 0$. This marks the formation of polariton condensation, in which a macroscopic number of particles occupy the same quantum state. It should be noted that polariton condensation is a non-equilibrium process and not a true Bose–Einstein condensate, since polaritons have a finite lifetime and require continuous optical pumping to maintain a steady-state population [66].

Above threshold, the condensate emits a bright, spectrally narrow, and temporally coherent light field known as polariton lasing. Unlike conventional photon lasing, this coherence emerges without population inversion, arising instead from spontaneous phase locking and collective occupation of the ground state. Experimentally, condensation is identified by a nonlinear increase in emission intensity, spectral line narrowing, and the appearance of long-range spatial and temporal coherence [22, 26, 63, 64].

4.3.2 Signatures of polariton lasing

Polaritons provide a lasing pathway in the strong-coupling regime, where coherent emission arises from stimulated scattering into the lowest-energy states of the LP branch, without requiring population inversion. In practice, polariton lasing is identified by a combination of signatures: a clear nonlinear threshold in LPB emission intensity accompanied by linewidth narrowing, a redistribution of emission toward low in-plane momentum ($k_{\parallel} \approx 0$), and the persistence of polaritonic emission (i.e., retention of strong coupling) above threshold [22, 26, 63, 65]. Additional supporting evidence can include the build-up of first-order coherence and characteristic nonlinear energy shifts of the LPB under increasing excitation density.

4.4 Polariton lasing in fully solution-processed microcavities

Organic polaritons offer an alternative route to coherent light generation that can operate at room temperature and at comparatively low thresholds, enabled by strong light–matter coupling in optical microcavities. A major practical limitation, however, is that while many organic polariton lasers employ solution-processed emitters, the cavity mirrors are typically fabricated using vacuum deposition, which increases cost and limits scalability. Building on the fully solution-processed dielectric microcavity platform introduced earlier, Publication 3 demonstrates that coherent nonlinear emission can be achieved in microcavities fabricated entirely by solution-based methods, establishing a scalable route toward low-cost polaritonic devices.

The devices investigated in Publication 3 are fully solution-processed organic microcavities consisting of polymeric distributed Bragg reflectors (TiOH/PVA and Nafion) and a spin-coated organic emitting layer. The cavity design supports strong light–matter coupling under non-resonant optical excitation, enabling access to the

nonlinear emission regime characteristic of polariton lasing. The samples were excited non-resonantly at 380 nm, and the emission was characterized using angle-resolved and real-space microspectroscopy, as described in Chapter 6.

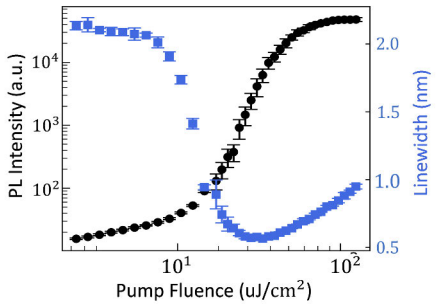

Figure 12. Evolution of emission intensity (black circles) and linewidth (blue squares) as a function of excitation fluence for a fully solution-processed microcavity adapted from Publicaiton III. A clear threshold is observed near $\sim 10\ \mu$J/cm^2, marking the onset of polariton lasing. Above threshold, the emission intensity exhibits a nonlinear increase, while the linewidth collapses, indicating the onset of temporal coherence and macroscopic occupation of the ground polariton state.

Under non-resonant optical excitation at room temperature. The devices exhibit a clear nonlinear emission threshold at an absorbed fluence of approximately 20 µJ cm^{-2}, accompanied by a pronounced narrowing of the LP linewidth and a macroscopic occupation of states near $k_{\parallel} \approx 0$. Below threshold, the emission follows the LP dispersion and increases linearly with pump fluence, while above threshold a superlinear intensity increase and linewidth reduction to less than $\sim$1 meV are observed, marking the onset of coherent polariton emission (Figure 12).

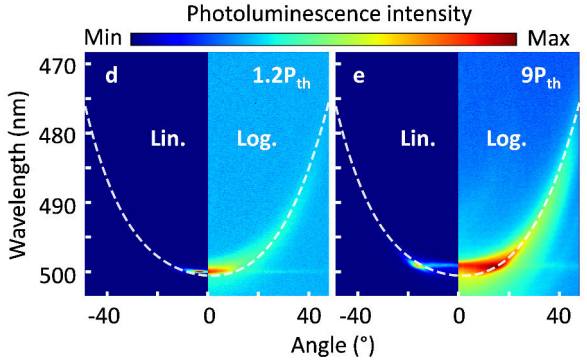

Figure 13. Angle-resolved emission maps at (d) 1.2P_{th} and (e) 9P_{th} adapted from Publicaiton III. With increasing excitation power, the polariton emission exhibits a continuous blueshift and redistribution toward higher in-plane momenta, while remaining on the LP branch dispersion (white dashed line). The persistence of the LPB and absence of mode collapse confirm that lasing occurs in the strong coupling regime.

Angle-resolved measurements in Figure 13 show that, above threshold, the emission remains on the LP branch and does not shift to the bare cavity mode or to exciton emission [65, 66]. With increasing excitation density, the polariton emission exhibits a small blueshift and gradually redistributes toward finite in-plane momenta. At high pump powers, this redistribution results in symmetric emission at off-normal angles, forming a characteristic momentum-space pattern while strong coupling is preserved.

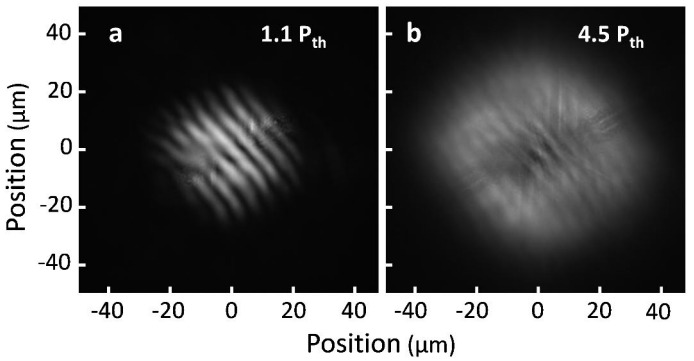

Figure 14. Real-space interferograms obtained in a Michelson interferometer configuration at (a) $1.1P_{\text{th}}$ and (b) $4.5P_{\text{th}}$ adapted from Publicaiton III. Just above threshold, well-defined interference fringes indicate the formation of a spatially coherent polariton condensate. At higher excitation fluences, fringe visibility decreases due to increased interactions and phase fluctuations within the condensate.

The important feature of polariton lasing is the emergence of long-range spatial coherence above threshold [22, 26, 64]. To probe this, a Michelson interferometer in the retro-reflector configuration was used, in which the cavity emission is overlapped with a spatially inverted replica of itself. Above the lasing threshold, high-contrast off-axis interference fringes appear, demonstrating the build-up of first-order spatial coherence and the macroscopic occupation of the $k \approx 0$ polariton mode in the solution-processed microcavity (Figure 14). The coherence extends across the excitation area and weakens at higher excitation densities, consistent with increased polariton–polariton interactions.

Real-space imaging shows that the condensate dynamics change with increasing pump power Figure 15 (a,b,c). Below threshold, the emission follows the Gaussian profile of the excitation beam. At threshold, the emission becomes localized at the center of the pump spot, while at higher excitation densities it redistributes outward, forming an annular emission pattern. Spatially resolved input–output measurements shown in Figure 15 (d) indicate that the emission at the pump center saturates, whereas regions farther from the center continue to increase in intensity. The observed annular emission pattern may arise from a repulsive interaction between the polariton population and the exciton reservoir, which could drive polariton emission

away from regions of high exciton density. Such spatial redistribution may reduce local exciton saturation at the pump centre and thereby help preserve the strong-coupling regime at elevated excitation fluences. Similar outward polariton flow and annular intensity distributions have been reported previously in inorganic polariton systems, such as GaAs and ZnO microcavities, typically under spatially structured or ring-shaped excitation conditions [67]. In the present case, however, the annular lasing emerges under uniform, non-structured excitation, suggesting that a different mechanism may contribute to the observed behaviour. Control experiments exclude material degradation, indicating that the spatial redistribution is an intrinsic feature of the polariton emission in these structures. A detailed quantitative analysis of the underlying reservoir-polariton dynamics is beyond the scope of the present work.

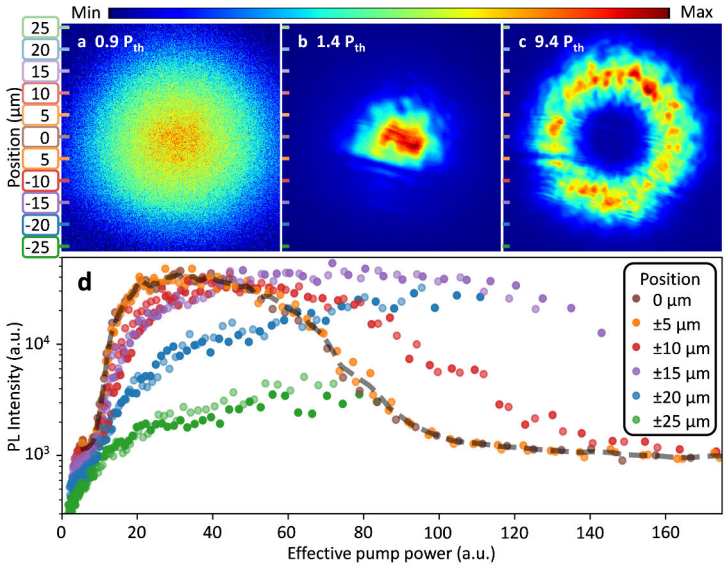

Figure 15. Real-space evolution of the polariton condensate under Gaussian pumping at different excitation powers adapted from Publicaiton III. (a–c) Below threshold ($0.9P_{\text{th}}$), the emission follows the pump profile; just above threshold ($1.4P_{\text{th}}$), the condensate localizes at the center; and at high excitation ($9.4P_{\text{th}}$), the emission redistributes outward to form an annular profile. (d) Power-dependent emission intensity extracted at increasing radial positions from the pump center. The central region saturates at high fluence, while off-center positions brighten with higher effective thresholds, consistent with outward flow driven by repulsive polariton–reservoir interactions.

In addition to coherence and macroscopic occupation of the ground state, thermalization of the polariton population provides further evidence for the formation of a condensate [65, 66]. For this, we analyse of the high-energy tail of the emission spectra that reveals a progressive cooling of the polariton population with increasing excitation density, with effective temperatures decreasing from approximately 480 K to near room temperature. This behavior indicates efficient energy relaxation

and quasi-thermalization of the condensate, driven by density-dependent scattering processes.

Taken together, these observations establish polariton lasing and condensate formation in microcavities fabricated entirely by solution-based methods. They highlight strong light–matter coupling as a key enabler of coherent emission in fully solution-processed vertical microcavity architectures. More broadly, these results show that simple and energy-efficient fabrication routes, when combined with appropriate material selection, can access new regimes of polariton behavior and provide a scalable platform for future classical and quantum photonic devices.

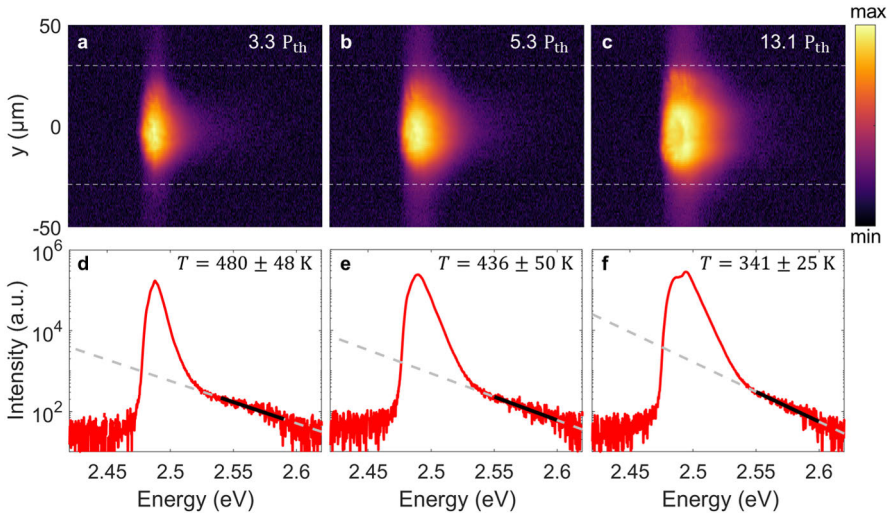

Figure 16. Thermalization of the polariton condensate adapted from Publicaiton III. (a–c) Real-space emission profiles at excitation powers of $\sim 3.3 P_{\text{th}}$, $\sim 5.3 P_{\text{th}}$, and $\sim 13.1 P_{\text{th}}$. (d–f) Corresponding emission spectra with Maxwell–Boltzmann fits (gray dashed lines), showing effective temperatures of 480 K, 436 K, and 341 K, respectively. The progressive cooling of the polariton distribution with increasing pump fluence evidences quasi-equilibrium condensation and efficient energy relaxation within the polariton ensemble.

In this chapter, we have demonstrated the realization of polariton lasing in fully solution-processed organic microcavities, highlighting the potential of low-cost, scalable fabrication for coherent light generation at room temperature. Building upon the theoretical framework of exciton–polariton condensation, we identified clear experimental signatures of polariton lasing, including nonlinear emission intensity, linewidth narrowing, energy blueshift, momentum-space condensation, coherence build-up, and thermalization. The persistence of strong coupling above threshold confirmed that lasing occurred within the polaritonic regime rather than through conventional photon lasing. Furthermore, real-space imaging revealed rich condensate dynamics, such as outward redistribution and annular flow driven by polariton–polariton repulsion, underscoring the complex interplay between interactions and spatial confinement in organic systems. Together, these results establish solution-processed microcavities as a versatile and robust platform for studying nonequilibrium condensates and advancing polariton-based photonic technologies.

5 Polariton optoelectronics

Note: This chapter summarizes the work presented in Publications IV and V, which investigate microcavity OLEDs and polariton-mediated excitonic processes.

The field of polariton optoelectronics seeks to merge the physics of strong light–matter coupling with the functionality of organic semiconductor devices. As discussed earlier, organic materials offer remarkable flexibility in tailoring electronic and optical properties through molecular design and synthetic chemistry, enabling the realization of a new class of emitters, photodetectors, and lasers [33, 66]. In particular, OLEDs have transformed modern display and lighting technologies [51, 68–70].

Understanding the nature of electronic excitations in organic semiconductors is therefore essential to linking fundamental excitonic processes with polaritonic and device-level phenomena. This chapter introduces the electronic excited states in organic molecules, emphasizing the formation and dynamics of singlet and triplet excitons, and discusses their significance in the operation and efficiency of OLEDs.

5.1 Organic Light–Emitting Diodes (OLEDs)

OLEDs are among the most prominent applications of organic semiconductors, owing to their low fabrication cost, flexibility, and ability to cover the full visible spectrum [32, 68, 70, 71]. Their operation relies on the recombination of electrons and holes in an emissive organic layer to generate excitons, which subsequently decay radiatively to emit photons.

5.1.1 Device structure and operation

A typical OLED consists of a multilayer structure deposited between two electrodes: a transparent anode (often indium tin oxide, ITO) and a reflective cathode (typically aluminium, silver, or a low-work-function alloy) [72, 73]. Between these electrodes, several organic layers are stacked to facilitate charge injection, transport, and recombination [71, 74]. A common configuration includes:

- a **hole-injection layer (HIL)** to assist hole injection from the anode,
- a **hole-transport layer (HTL)** to convey holes toward the emissive region,
- an **emissive layer (EML)** where recombination and light emission occur,

- an **electron-transport layer (ETL)** to deliver electrons toward the EML,
- and sometimes an **electron-injection layer (EIL)** to facilitate charge transfer from the cathode.

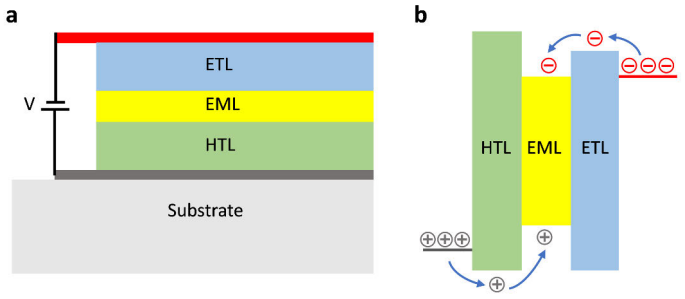

Figure 17. Schematic structure and charge transport in a multilayer OLED. (a) Layer arrangement of a typical OLED device, consisting of a HTL, an EML, and an ETL sandwiched between two electrodes. (b) Illustration of charge injection and recombination: holes (gray circles) are injected from the anode and transported through the HTL, while electrons (red circles) are injected from the cathode and transported through the ETL. Charge carriers meet and recombine in the EML to form excitons that subsequently emit light.

When a bias voltage is applied across an OLED, electrons are injected from the cathode into the ETL, while holes are injected from the anode into the HTL. These transport layers facilitate the movement of charge carriers by providing energetically favorable pathways and blocking the opposite charge to ensure efficient confinement. Electrons drift through the ETL toward the EML, while holes migrate through the HTL in the opposite direction. At the HTL/EML and ETL/EML interfaces, energy level alignment enables efficient carrier injection into the EML, where electrons and holes meet to form bound electron–hole pairs (excitors). Exciton formation and recombination occur primarily within the EML, whose composition and thickness are engineered to maximize radiative recombination and minimize losses [69, 71]. Additional layers, such as hole-blocking layers (HBL) or electron-blocking layers (EBL), may be incorporated to prevent carriers from leaking out of the emissive region, thereby improving charge balance and device efficiency. The radiative decay of excitons within the EML produces photons, which propagate through the device stack and are extracted as visible light.

5.1.2 Efficiency parameters

The efficiency of an OLED is typically quantified in terms of its internal and external quantum efficiencies. The **internal quantum efficiency (IQE)** describes the ratio of emitted photons to injected charge carriers within the device:

$$\eta_{\mathrm{IQE}} = \eta_{\mathrm{r}} \times \eta_{\mathrm{PLQY}} \times \eta_{\mathrm{ST}}, \tag{34}$$

where η_{r} is the charge-balance factor, η_{PLQY} is the photoluminescence quantum yield of the emissive layer, and η_{ST} represents the fraction of excitons that can decay radiatively (25% for fluorescent emitters and up to 100% for phosphorescent or TADF systems) [51, 75–77].

However, not all generated photons escape the device due to optical losses caused by total internal reflection and waveguiding within the organic layers. The **external quantum efficiency (EQE)** accounts for this outcoupling efficiency (η_{out}):

$$\eta_{\mathrm{EQE}} = \eta_{\mathrm{IQE}} \times \eta_{\mathrm{out}}. \tag{35}$$

In conventional planar OLEDs, η_{out} is typically around 20–30% [71, 78], meaning that even highly efficient emissive systems can lose up to 70–80% of the generated light to trapped modes.

5.2 Molecular orbitals and electronic excitation

In molecules, atomic orbitals (AOs) from the constituent atoms combine to form molecular orbitals (MOs) through the linear combination of atomic orbitals (LCAO) principle [79]. When two atomic orbitals, ψ_A and ψ_B, overlap, they form a bonding and an antibonding orbital:

$$\psi_{\text{bonding}} = \psi_A + \psi_B, \qquad \psi_{\text{antibonding}} = \psi_A - \psi_B. \tag{36}$$

Constructive interference increases electron density between the nuclei and stabilizes the bonding orbital, whereas destructive interference creates a node and results in a higher-energy antibonding orbital.

Electrons fill these orbitals according to the Pauli exclusion principle and Hund's rule. The Pauli exclusion principle states that no two electrons can possess the same set of quantum numbers $(n,\, l,\, m_l,\, m_s)$; therefore, each orbital can hold at most two electrons with opposite spins. Hund's rule dictates that in degenerate orbitals, electrons occupy separate orbitals with parallel spins to minimize Coulomb repulsion.

The highest occupied molecular orbital (HOMO) is the uppermost filled orbital, while the lowest unoccupied molecular orbital (LUMO) is the lowest available empty orbital. The energy difference between them,

$$E_{\text{gap}} = E_{\text{LUMO}} - E_{\text{HOMO}}, \tag{37}$$

defines the optical bandgap and strongly influences the absorption and emission spectrum of the molecule [74].

When a photon of energy $h\nu \geq E_{\text{gap}}$ is absorbed, an electron is promoted from the HOMO to the LUMO, leaving behind a hole. The electron and hole remain bound by Coulomb attraction, forming a neutral quasiparticle known as an *exciton*. The formation and relaxation of such excitons underpin the photophysical behaviour of organic semiconductors, OLEDs, and polaritonic microcavities [74, 79].

5.3 Singlet and triplet excited states

Photoexcitation in organic semiconductors promotes an electron from the HOMO to the LUMO, creating a Coulomb-bound electron–hole pair known as an exciton. Due to the low dielectric constant of organic materials, these excitons are tightly bound ($\sim$0.5–1 eV) and typically localized on individual molecules [74, 79].

Depending on the relative spin alignment of the electron and hole, two distinct excited-state manifolds can be formed:

- **Singlet excitons** ($S = 0$)**:** Spins are antiparallel, resulting in a total spin of zero. Radiative decay to the ground state is spin-allowed, giving prompt fluorescence with lifetimes on the nanosecond scale [74, 79].

- **Triplet excitons** ($S = 1$)**:** Spins are parallel, giving rise to three degenerate substates ($M_S = -1, 0, +1$). Radiative decay is spin-forbidden, leading to long lifetimes (microseconds–milliseconds) and dominant non-radiative decay channels unless strong spin–orbit coupling enables phosphorescence [77].

The formation statistics depend on the excitation mechanism. Under optical excitation, photon absorption preserves spin, and the initially formed state is a singlet exciton; triplets arise only via ISC [79]. Because optical excitation preserves spin, triplet excitons do not form directly but only through ISC, typically with rates ranging from picoseconds to nanoseconds depending on molecular structure [74, 80]. Under electrical excitation, electron–hole capture is spin random and produces a statistical 1:3 ratio of singlet to triplet excitons:

$$P_S : P_T = 1 : 3. \tag{38}$$

which imposes a 25% upper limit on the internal quantum efficiency of purely fluorescent OLEDs [81].

5.4 Relaxation mechanisms in organic semiconductors

Once an exciton is formed, it may relax through several radiative and non-radiative pathways, which are summarized in the simplified Jablonski diagram in Figure 18.

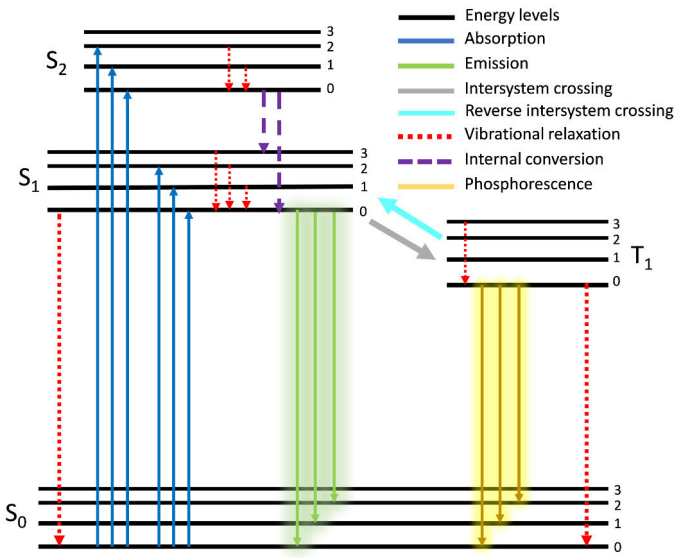

Figure 18. Simplified Jablonski diagram showing the key relaxation pathways of singlet and triplet excitons in organic semiconductors, including fluorescence, internal conversion (IC), vibrational relaxation, ISC, RISC and phosphorescence.

Singlet excitons (S_1) may decay directly to the ground state (S_0) via prompt fluorescence on nanosecond timescales, or undergo non-radiative internal conversion (IC) [79]. Triplet excitons (T_1), formed either through ISC or via electrical excitation, are spin-forbidden from returning directly to S_0, resulting in long lifetimes (microseconds–milliseconds) and dominant non-radiative decay unless additional mechanisms intervene [77].

Several pathways allow triplet excitons to contribute to delayed light emission:

- **Phosphorescence:** In heavy-metal complexes (e.g. Ir(III), Pt(II)), strong spin–orbit coupling (SOC) relaxes the spin selection rule and enables radiative decay from $T_1 \rightarrow S_0$. This mechanism enables nearly 100% internal quantum efficiency in phosphorescent OLEDs [51, 77].

- **Thermally Activated Delayed Fluorescence (TADF):** In donor–acceptor molecules with a small singlet–triplet energy gap (ΔE_{ST}), thermal activation can return triplet excitons to S_1 through RISC, leading to delayed fluorescence without heavy atoms [75, 76]. The gap is determined mainly by the electron–hole exchange interaction:

$$\Delta E_{ST} \approx 2J, \tag{39}$$

  where J is minimized by spatially separating HOMO and LUMO wavefunctions [75, 76].

- **Triplet–Triplet Annihilation (TTA):** Two triplet excitons may interact to produce one higher-energy singlet exciton:

$$T_1 + T_1 \rightarrow S_1 + S_0,$$

  resulting in delayed fluorescence with a maximum theoretical efficiency of 50%. TTA is prominent in materials with long triplet lifetimes and high triplet densities [51, 80].

- **Trap States Delayed Emission:** Triplets can be transiently captured at defect sites and later released, producing weak long-lived emission. While generally undesirable, such processes can influence recombination dynamics in disordered organic films [80].

The characteristic rates of these processes span many orders of magnitude, from sub-picosecond internal conversion to millisecond-scale phosphorescence. Table 2 summarizes the typical timescales associated with key radiative and non-radiative pathways in organic semiconductors [74, 77, 79, 80].

Table 2. Typical timescales of relaxation pathways in organic semiconductors.

Process	**Mechanism**	**Typical Timescale**
Prompt fluorescence	$S_1 \rightarrow S_0$ (radiative)	0.1 - 10 ns
IC	$S_1 \rightarrow S_0$ (non-radiative)	100 fs - 10 ps
ISC	$S_1 \rightarrow T_1$	1 ps - 100 ns
Phosphorescence	$T_1 \rightarrow S_0$ (radiative)	1 μs - 10 ms
Reverse ISC (RISC, TADF)	$T_1 \rightarrow S_1$	100 ns - 100 μs
Triplet-triplet annihilation (TTA)	$T_1 + T_1 \rightarrow S_1$	μs - ms (density dependent)
Delayed fluorescence (TADF/TTA)	$S_1 \rightarrow S_0$ (radiative)	100 ns - ms
Trap-state emission	Defect-bound excitons	μs - seconds

These competing radiative and non-radiative channels govern the usable exciton population in OLEDs, polaritonic microcavities, and other organic optoelectronic systems. Understanding how to either harvest or suppress triplet states is therefore central to the design of high-efficiency organic emitters and devices.

The prospect of using strong light–matter coupling to reshape molecular energy landscapes has motivated extensive research into polariton chemistry, where the hybridization between excitons and confined photons creates new eigenstates that may influence photophysical rates [13, 32–39]. One process of particular relevance to OLEDs is RISC, in which triplet excitons convert into singlets. In principle,

tuning the LP energy relative to the molecular triplet level could modify the energetic driving force for such transitions, thereby altering delayed emission dynamics. However, the collective nature of strong coupling in organic films means that any polariton-induced modification of intramolecular processes may be strongly diluted at the single-molecule level [34, 35]. Moreover, most prior studies probing polariton effects on RISC have been performed under optical excitation in TADF emitters, where intrinsically fast triplet harvesting often obscures subtler cavity-induced influences [32–35].

Publication IV therefore investigates a complementary regime: electrically driven POLEDs based on a purely fluorescent emitter, TDAF, which has a large singlet–triplet splitting ($\Delta E_{S_1-T_1} \approx 0.8$ eV) rendering RISC negligible [75, 76]. Electrical injection naturally generates a 3:1 ratio of triplets to singlets, providing a substantial triplet reservoir directly within the device. TDAF is also an ideal material for this study due to its high oscillator strength—enabling Rabi splittings near 0.9 eV—and its ambipolar transport, which allows the emitting layer to be placed directly between the charge injection layers, producing a simple and uniform OLED microcavity structure (Figure 19).

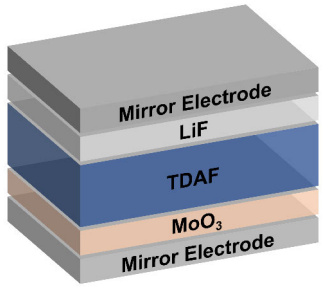

Figure 19. Cross-sectional architecture of the POLED, consisting of a bottom mirror contact/MoO_3/TDAF/LiF/top mirror contact adapted from Publicaiton IV.

Three POLEDs were fabricated in which the TDAF thickness was varied to tune the LP energy progressively toward the molecular triplet level. Angle-resolved reflectivity confirmed ultrastrong coupling, with vacuum Rabi splittings of 0.92, 0.88, and 0.96 eV (Figure 20). The large splitting ensures that the LP maintains substantial excitonic character even under strong negative detuning, a prerequisite for any potential polariton–triplet interaction.

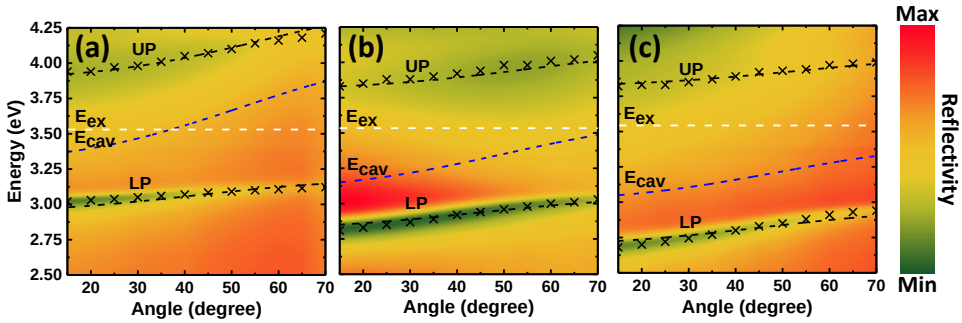

Figure 20. Angle-resolved reflectivity for three microcavity OLEDs with progressively increasing negative detuning adapted from Publicaiton IV. Dark dispersive bands correspond to the LP and UP polariton branches. The dashed blue line marks the bare cavity mode ω_{cav}, while the dashed white line indicates the exciton energy ω_{ex}. Dashed curves show coupled-oscillator fits. From (a) to (c), increasing negative detuning lowers the LP energy (2.95, 2.83, and 2.67 eV at normal incidence), shifting the LP closer to the triplet.

To probe whether aligning the LP energy with the triplet manifold influences excited-state dynamics, time-resolved electroluminescence (TREL) was performed under pulsed electrical excitation. A reference OLED with an ITO anode was first examined. Its EL decay exhibited a delayed component dominated by trap-assisted emission rather than TTA or TADF, consistent with the absence of efficient RISC in TDAF (Figure 21). This established a baseline against which the polaritonic devices could be compared .

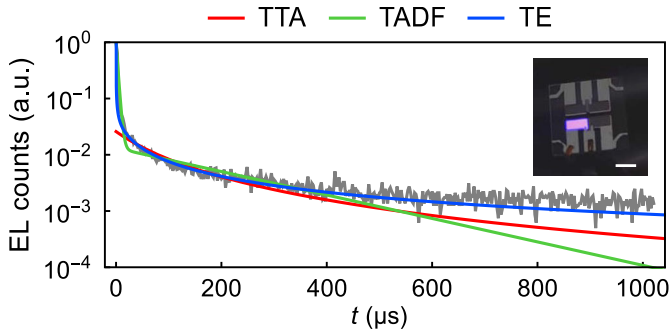

Figure 21. Adapted from Publicaiton IV, semi-logarithmic time-resolved electroluminescence (gray) recorded after bias turn-off, together with rate-equation fits decomposed into contributions from thermally activated delayed fluorescence (TADF, green), triplet–triplet annihilation (TTA, red), and trap-assisted emission (TE, blue). The fit indicates that trap emission dominates the delayed component.

TREL measurements of the three POLEDs revealed that the delayed electroluminescence traces are essentially unchanged across devices, despite systematically reducing the LP–triplet energy separation (Figure 22). This behavior persisted across a wide current range (30–150 mA.cm^{-2}), with only minor current-dependent quench-

ing effects. Rate-equation modelling showed that the delayed EL in all devices is dominated by trap-state recombination, with no evidence for a TADF-like channel (triplet→LP→singlet) or a direct trap→LP transition. Within the resolution of the experiment, strong coupling does not measurably alter triplet-harvesting pathways in TDAF.

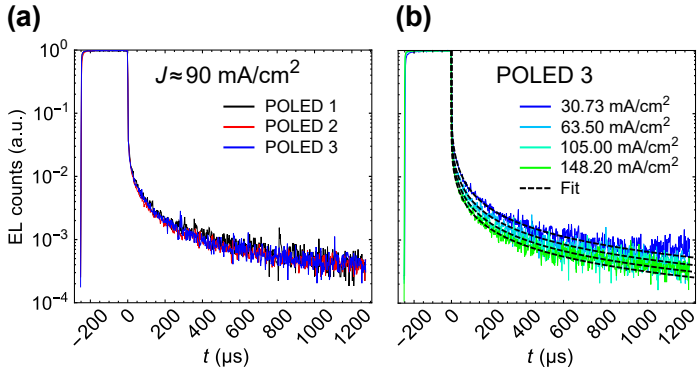

Figure 22. Time-resolved electroluminescence (TREL) following bias turn-off adapted from Publicaiton IV. (a) Decay traces for POLEDs 1-3 measured at an injection current of $\approx 90\ \mathrm{mA\,cm^{-2}}$ exhibit nearly identical delayed-emission profiles despite their different detunings. (b) TREL of POLED 3 recorded at 30.7, 63.5, 105.0, and 148.2 $\mathrm{mA\,cm^{-2}}$; dashed lines show rate-equation fits. The long-time decay tail varies only weakly with current, with modest quenching observed at higher drive levels.

These results indicate that, although strong coupling is robustly achieved, tuning the LP near the triplet manifold does not modify delayed emission dynamics in this fluorescent emitter. A likely explanation is the collective nature of polaritons: the photonic component is delocalized over N molecules, reducing its effective interaction with any individual triplet or trap state by a factor $\sim 1/N$ [34, 35]. As a result, even when energetics appear favorable, cavity-assisted triplet harvesting remains too weak to detect.

Overall, Publication IV demonstrates that in electrically driven POLEDs based on TDAF, strong coupling substantially reshapes the photonic environment yet does not induce observable modifications to triplet population dynamics. Whether polaritons can influence triplet behavior more broadly remains an open question and will likely require systematic studies using emitters with intrinsically slow or tunable RISC, well-defined TTA pathways, or strongly localized triplet states.

5.5 Metal-clad microcavity engineering for single-component white OLEDs (WOLEDs)

OLEDs are central to modern display and lighting technologies, yet their widespread adoption in solid-state lighting remains constrained by fabrication complexity, colour

instability, and reliance on transparent electrodes such as indium–tin oxide (ITO). Conventional WOLEDs typically employ multiple emitter (red, green, and blue) either spatially separated or blended, requiring precise control of exciton distribution and often exhibiting colour drift due to differential aging of the emitters. Single-component WOLEDs circumvent these challenges, but they rely on synthetically demanding emitters with multi-resonant or aggregation-induced emission and remain rare in practice. These limitations motivate alternative strategies that use photonic engineering, rather than molecular design, to achieve broadband white emission from a single, efficient blue emitter.

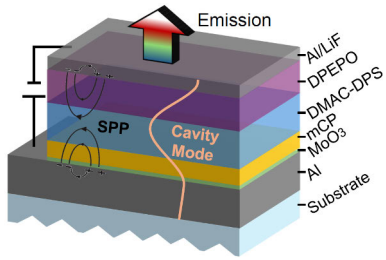

Figure 23. (a) Schematic illustration of the Al-clad microcavity OLED used for spectral engineering of a neat DMAC-DPS emitting layer adapted from Publicaiton V. The architecture consists of an Al bottom electrode, MoO_3 hole-injection layer, mCP hole-transport layer, DMAC-DPS emitter, DPEPO electron-transport layer, and a thin Al/ LiF top electrode. The combination of a weak cavity mode and surface plasmon polariton (SPP) modes at the metal/dielectric interfaces redistributes the DMAC-DPS emission across the visible spectrum.

In Publication 5, we introduce a simple and scalable metal-clad microcavity architecture as shown in Fig. 23 that converts the intrinsically blue electroluminescence of the TADF emitter DMAC-DPS into spectrally tunable white light without using ITO or multi-emitter systems. The device comprises a highly reflective 70 nm Al bottom electrode, a neat DMAC-DPS emissive layer of adjustable thickness, standard charge-transport layers, and an ultrathin 15 nm Al top electrode acting simultaneously as the semi-transparent outcoupling mirror and the electrical cathode. DMAC-DPS is an ideal platform for this approach due to its high internal quantum efficiency, broad photoluminescence spectrum (420–650 nm), and established performance in blue OLEDs. By varying the thickness of the DMAC-DPS layer, the effective cavity length is tuned so that a weak cavity mode is placed at different regions of the DMAC-DPS emission spectrum, enabling controlled spectral redistribution via cavity filtering and radiative-rate modification.

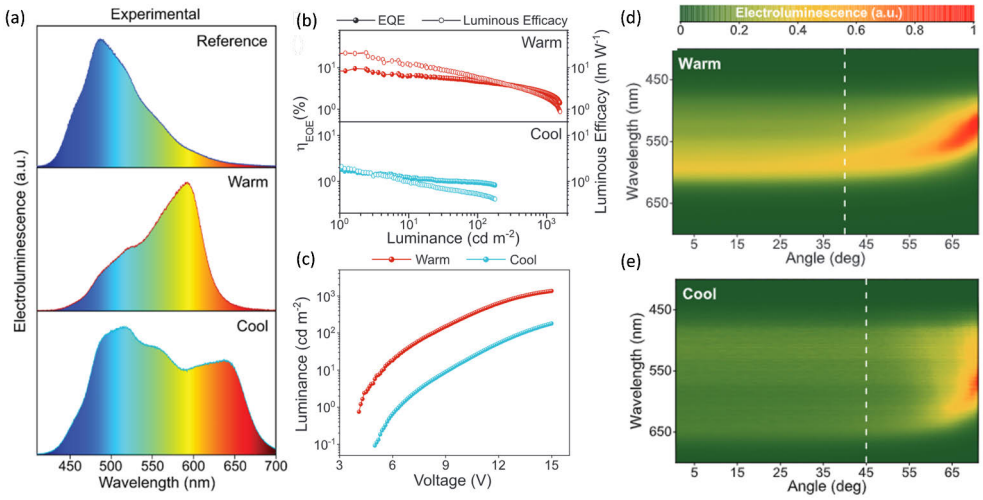

Figure 24. Optical and electrical performance of reference and microcavity WOLEDs adapted from Publicaiton V. (a) Normalized experimental electroluminescence (EL) spectra of the reference BEOLED and microcavity WOLEDs with warm ($d_{\mathrm{EML}} = 55$ nm) and cool ($d_{\mathrm{EML}} = 75$ nm) emission. (b) External quantum efficiency η_{EQE} (filled circles) and luminous efficacy (open circles) as a function of luminance for the warm and cool WOLEDs. (c) Luminance as a function of applied voltage for the warm ($d_{\mathrm{EML}} = 55$ nm) and cool ($d_{\mathrm{EML}} = 75$ nm) WOLEDs. (d,e) Contour plots of normalized angle-resolved electroluminescence for the (d) warm and (e) cool WOLEDs. The dashed white lines indicate the emission angles at which the relative spectral shift $\Delta\lambda$ reaches 1%.

Using the DMAC-DPS structure previously optimized for high efficiency [75], we first demonstrate cavity-enhanced narrowband blue emission (500 nm, FWHM 40 nm, EQE 14%) and green emission (555 nm, EQE 10%). Increasing the emissive-layer thickness further detunes the cavity resonance toward the red tail of DMAC-DPS, producing broadband white emission from a single emitter. Devices with 55 nm and 75 nm emissive layers yield warm (CCT 3790 K) and cool (CCT 4440–5050 K) white spectra with FWHM values up to 190 nm Fig. 24 (a), and external quantum efficiencies of up to 4.7% as shown in Fig. 24 (b,c). The white emission remains highly angle-stable, with chromaticity variations below 3% over viewing angles exceeding $\pm 40^{\circ}$ (Figure 24(d,e)), a notable advantage over multi-emitter WOLEDs where spectral balance depends sensitively on current density and recombination pathways.

The underlying spectral broadening originates from the combined action of a low-Q cavity mode and surface plasmon polariton (SPP) modes supported by the thin Al electrodes. Optical simulations using a classical dipole model and TMM reproduce the measured spectra with excellent agreement (Fig. 25a) and reveal that cavity filtering (via the outcoupling function $P_{\mathrm{out}}(\lambda)$) and radiative-rate enhancement ($EF(\lambda)$) jointly determine the final electroluminescence. Transient photoluminescence measurements shown in Fig. 25(b,c,d) support this interpretation: the

prompt lifetime of DMAC-DPS decreases from 20.2 ns in a neat film to 17.3 ns in the warm-white microcavity OLED, consistent with moderate radiative-rate enhancement, while the delayed lifetime is also shortened (1.4 µs vs 2.4 µs), which attribute to increased triplet quenching in the device environment.

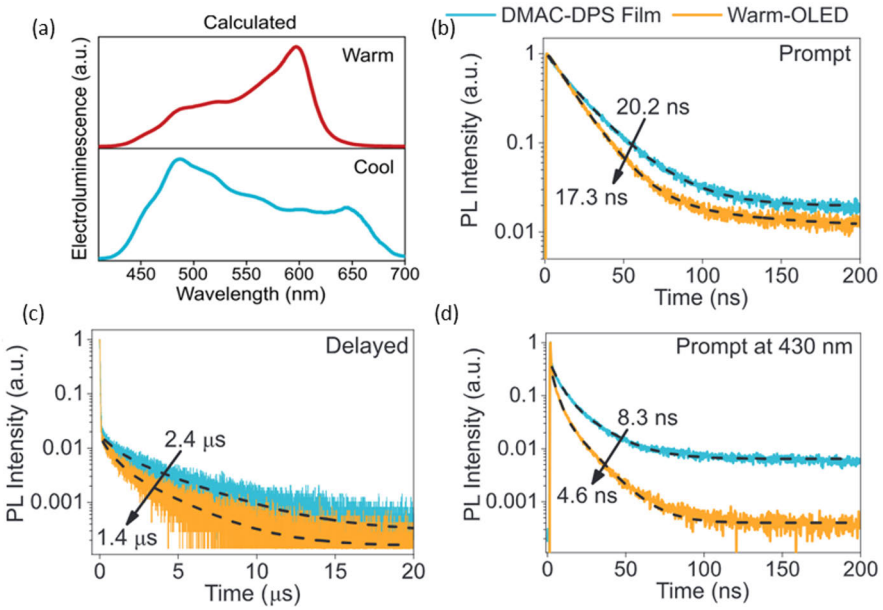

Figure 25. Calculated electroluminescence spectra and time-resolved photoluminescence dynamicsadapted from Publicaiton V. (a) Calculated normalized electroluminescence spectra of the top-emitting WOLEDs, $T_{\mathrm{EL}}(\lambda)$, obtained as $T_{\mathrm{EL}}(\lambda) = E_F(\lambda) \times P_{\mathrm{out}}(\lambda) \times B_{\mathrm{EL}}(\lambda)$, where $B_{\mathrm{EL}}(\lambda)$ is the measured and normalized electroluminescence spectrum of the reference BEOLED. (b) Transient photoluminescence (TRPL) decay of a DMAC-DPS neat film (blue) and the warm WOLED (orange) under excitation at 370 nm, showing the prompt fluorescence component. (c) Delayed photoluminescence decay measured for the same samples, revealing microsecond-scale emission dynamics.The TRPL lifetimes in (b,c) were extracted from emission integrated over the wavelength range 480–620 nm. (d) Prompt fluorescence decay detected at 430 nm for the DMAC-DPS film and warm WOLED. Dashed lines represent double-exponential fits used to extract the characteristic lifetimes.

Although the efficiency of these devices remains limited by absorption in the ultrathin Al top electrode and charge imbalance for thicker DMAC-DPS layers, the demonstrated architecture offers several advantages: it eliminates the need for ITO, avoids multi-emitter complexity and achieves tunable, angle-stable white light emission with a single emissive material. Together, these results establish metal-clad microcavities as a highly practical and material-efficient route to single-component WOLEDs, providing new opportunities for large-area, low-cost, and sustainable solid-state lighting technologies.

In this chapter, we connected the fundamental excitonic processes of organic semiconductors with their behavior in optical microcavities and device architectures. Beginning with the operation of OLEDs, we highlighted how charge injection, exciton formation, and the balance between radiative and non-radiative pathways determine device efficiency. A detailed examination of singlet and triplet excited states, along with their relaxation mechanisms, established the framework necessary for understanding both conventional and polaritonic emission.

Building on this foundation, we explored how strong light–matter coupling can reshape the photonic environment of an emitter. Through the study of TDAF-based POLEDs, we examined whether tuning the LP toward the triplet manifold influences electroluminescence dynamics. Although a delayed emission component emerged in the microcavities, rate-equation analysis revealed that it originated from intrinsic trap-state recombination rather than cavity-assisted triplet harvesting. Strong coupling did not induce RISC or modify triplet behavior in this fluorescent system, underscoring the need for broader material studies to establish whether polariton modes can meaningfully influence triplet-related processes.

Finally, we demonstrated how optical engineering in the weak-coupling regime can be used to tailor emission without altering molecular structure. By embedding a neat DMAC-DPS film inside a metal-clad microcavity, we achieved single-component, ITO-free WOLEDs through cavity- and SPP-mediated spectral redistribution. The approach enables tunable white emission and simplified fabrication, revealing how photonic architectures can complement molecular design in optimizing device performance.

Together, these results illustrate how polariton physics and photonic engineering offer powerful tools for modifying exciton dynamics, enhancing light extraction, and shaping emission spectra in organic optoelectronics, while also highlighting open questions surrounding triplet management under strong coupling.

---

6 Materials and Experimental Methods

This chapter describes the materials, thin-film fabrication methods, microcavity assembly procedures, and optical characterisation techniques used throughout this thesis. Emphasis is placed on solution-processed multilayer structures, organic emitters, and the experimental setups required to investigate strong light–matter coupling and polariton dispersion. The theoretical principles behind key fabrication methods such as dip coating and spin coating are also introduced to provide the physical basis for the processing strategies adopted in this work.

6.1 Materials

A range of organic emitters with distinct photophysical properties were employed in this work. Their selection was guided by spectral compatibility with the microcavity design, film-forming behaviour, and suitability for solution or vacuum processing. The following subsections summarise their key optical characteristics and the rationale for their use in the experimental studies, while detailed fabrication procedures are presented later in this chapter.

Rhodamine 6G (R6G)

Rhodamine 6G (R6G) is a xanthene-based fluorescent dye widely used as a benchmark emitter due to its high photoluminescence quantum yield (PLQY), strong absorption in the green spectral region, and excellent solubility in polar solvents [82]. Its broad absorption and emission spectra make it an ideal material for probing cavity resonances and testing strong coupling conditions in solution-processed structures. In this thesis, R6G was embedded in PVA to form smooth thin films with high optical quality. Because both R6G and PVA are water-soluble, they are not intrinsically compatible with the aqueous dip-coating solutions used to deposit the DBR layers. To ensure compatibility, the R6G/PVA films were encapsulated with a thin Poly-TPD layer and then the sample edges were further sealed with UV-curable epoxy to prevent solvent diffusion through the edges during top DBR fabrication.

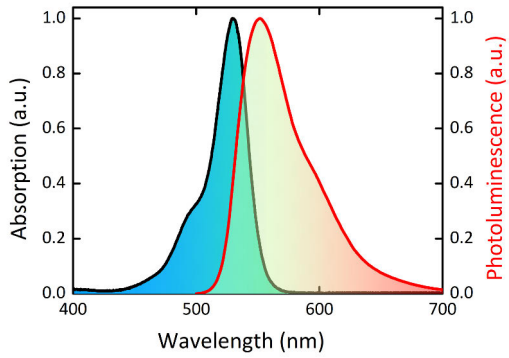

Figure 26. Absorption and emission spectra of Rhodamine 6G in a PVA matrix.

2,5-Bis[4-(diphenylamino)styryl]benzene (DPAVB)

DPAVB is a rigid, conjugated organic chromophore exhibiting strong π–π^* transitions in the blue–green spectral region [83]. It features high oscillator strength, a narrow emission spectrum, and reduced non-radiative losses due to its structural rigidity. These properties make DPAVB well suited for cavity–exciton coupling studies. In this work, DPAVB was blended with polystyrene (PS) to provide favourable film morphology and thickness control during spin coating.

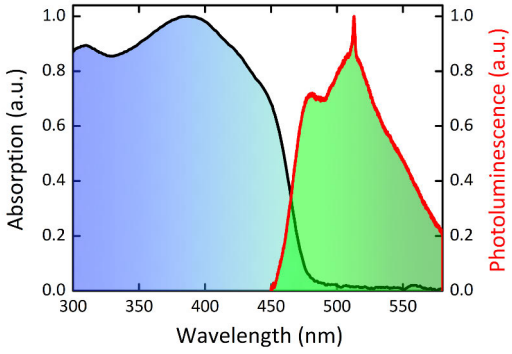

Figure 27. Absorption and emission spectra of DPAVB in a polystyrene matrix.

2,8-Bis(diphenylamino)-9,9-dimethylfluorene (TDAF)

TDAF is a blue-emitting small molecule characterised by high PLQY and strong fluorescence originating from singlet excitons [84]. Its large bandgap and high triplet energy render it suitable for use in both OLEDs and optical microcavities target-

ing the blue spectral region. In this thesis, TDAF was deposited via vacuum thermal evaporation to produce high-quality, smooth films for integration into hybrid metal–dielectric cavity structures.

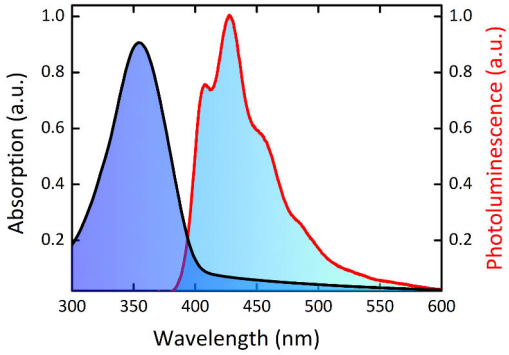

Figure 28. Absorption and emission spectra of a neat TDAF film.

DMAC/DPS (TADF emitter system)

The DMAC/DPS donor–acceptor system is a well-established thermally activated delayed fluorescence (TADF) emitter pair. It consists of an electron-donating acridine derivative (DMAC) and an electron-accepting sulfone (DPS). The small singlet–triplet energy splitting ($\Delta E_{\mathrm{ST}} \approx 0.1$ eV) enables efficient RISC, allowing triplet excitons to upconvert into emissive singlets [75]. This mechanism facilitates nearly unity internal quantum efficiency, making DMAC/DPS attractive for examining the interplay between triplet harvesting and strong light–matter coupling.

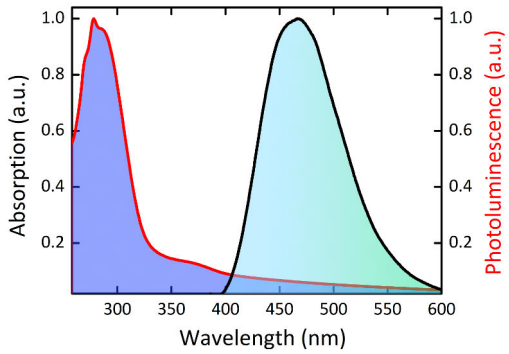

Figure 29. Absorption and emission spectra of a neat DMAC/DPS film.

TiOH/PVA hybrid high-index material

Titanium oxide hydrate/poly(vinyl alcohol) (TiOH/PVA) hybrid thin films served as the high-index material in the solution-processed DBRs. It was synthesized following the protocol by Russo et al. [85] by slowly hydrolyzing 2.2 mL of TiCl4 into 20 mL of cold H2O in an ice bath to hinder the formation of TiO2 nanoparticles and their aggregation. This cold solution was then combined 1:1 in volume with cold aqueous PVA (e.g., 15 g/L) to create the TiOH/PVA hybrid solution described by Bachevillier et al. [86]. The hydrolyzed titanium precursor forms a polymeric network of Ti–O–Ti bonds interlinked with hydroxyl groups, which act as scattering centers when uncontrolled but can be effectively suppressed through coordination with PVA chains. The addition of PVA not only enhances the structural integrity of the film but also provides uniform coverage, reduces cracking during drying, and ensures nanoscale thickness control across large areas. The optical constants extracted from ellipsometry measurements are shown in Fig. 30.

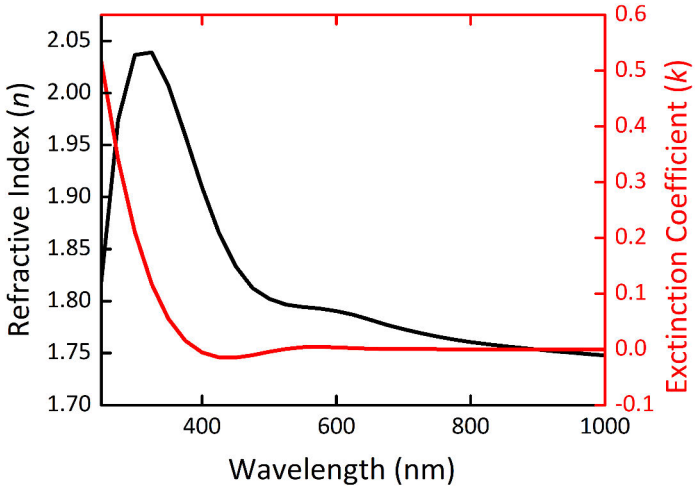

Figure 30. Refractive index $n(\lambda)$ and extinction coefficient $k(\lambda)$ of the TiOH/PVA hybrid film.

6.2 Fabrication techniques

6.2.1 Spin coating

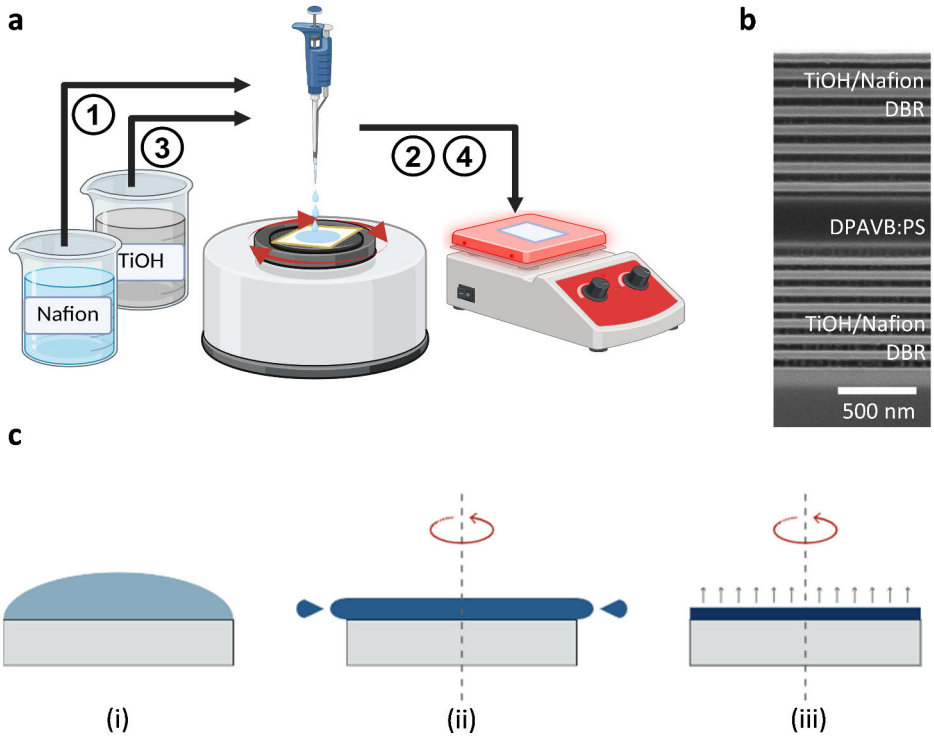

Figure 31. (a) Schematic of the fabrication sequence for a solution-processed TiOH/Nafion–DPAVB:PS-TiOH/Nafion microcavity. The TiOH/PVA and Nafion DBR stacks are first prepared by solution processing (1,3), after which the organic emitter layer is deposited by spin coating (2) and subsequently annealed on a hotplate (4). (b) Cross-sectional SEM image of the resulting structure, showing the TiOH/Nafion DBRs and the spin-coated DPAVB:PS layer. (c) Illustration of the spin-coating steps taken from Ref. [46]: (i) droplet deposition, (ii) spreading and thinning of the liquid film under rotation, and (iii) formation of a uniform solid film after solvent evaporation.

Spin coating was used to fabricate the organic emitter layers employed in publications II and III and DBRs in publication III. The overall process for integrating these layers into the solution-processed microcavities is illustrated in Fig. 31(a). The film formation sequence is sketched in Fig. 31(c). A liquid initially wets the substrate (i), then spreads and thins under the action of centrifugal forces during rotation (ii), and finally forms a uniform solid film after solvent evaporation (iii). The final film thickness is mainly controlled by the spin speed and follows the empirical scaling

$$h \propto \sqrt{\omega}, \tag{40}$$

where h is the film thickness and ω the angular rotation rate. Although solution viscosity, solute concentration, and solvent volatility also affect the outcome, adjusting the spin speed provides the most straightforward and reproducible way to tune film thickness in practice. Spin coating yielded smooth, homogeneous layers enabling the fabrication of high-quality microcavities. The specific processing parameters used for each material system are summarised in Table 3.

Table 3. Spin-coating parameters used for the fabrication of organic emitter layers in this thesis.

Material	Solvent / Host	Conc. (mg/mL)	Speed (rpm)	Time (s)	Annealing	Type
Rhodamine 6G	Methanol / PVA	1	2500	50	80°C / 2 min	Static
Rhodamine 6G	Methanol / PVA	3	2700	50	80°C / 2 min	Static
Rhodamine 6G	Methanol / PVA	5	3000	50	80°C / 2 min	Static
PolyTPD	Chlorobenzene	5	5000	50	100°C / 10 min	Dynamic
DPAVB	Toluene / PS	20	2000	40	60°C / 2 min	Dynamic
TiOH	Water / PVA	XX	4500	40	80°C / 2 min	Static
Nafion	IPA	XX	4500	40	80°C / 2 min	Dynamic

6.2.2 Dip coating

Dip coating was used to fabricate the TiOH/PVA and Nafion layers that form the solution-processed DBRs. The process is illustrated in Fig. 32(a), where the substrate is immersed into the precursor solution, withdrawn at a controlled speed, and subsequently annealed to remove residual solvent. A thin liquid film remains on the substrate during withdrawal due to the balance between capillary forces and viscous drag, as schematically shown in Fig. 32(c). After solvent evaporation, this forms a uniform solid layer suitable for multilayer optical stacks.

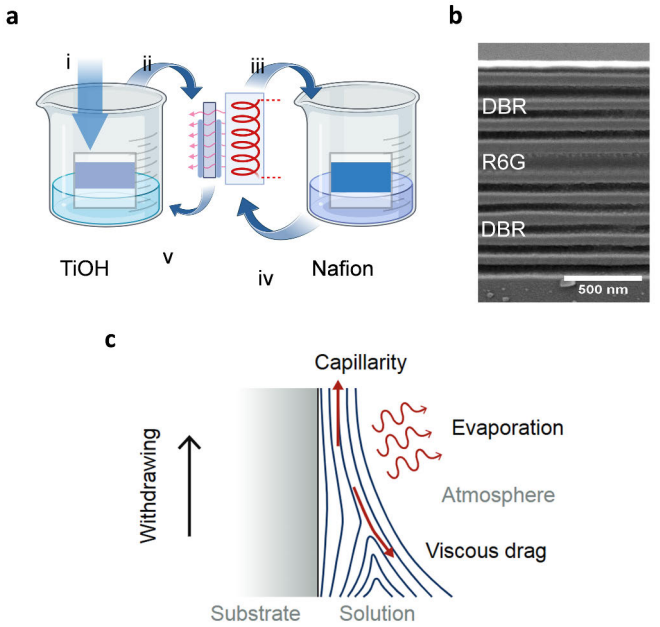

Figure 32. (a) Schematic of the dip-coating process for TiOH/PVA and Nafion layers, illustrating immersion, withdrawal, and annealing steps. (b) Cross-sectional SEM of a solution-processed DBR–R6G–DBR microcavity showing highly uniform TiOH/PVA–Nafion multilayers. (c) The process of dip coating taken from taken from Ref. [46]. Flow and force balance during withdrawal, highlighting the roles of capillarity, viscous drag, and solvent evaporation.

In the draining regime relevant to this work, the final film thickness is governed predominantly by the withdrawal speed and the viscosity of the coating solution. Faster withdrawal produces thicker layers, whereas excessively high speeds may lead to vertical thickness gradients; in such cases, increasing the solution viscosity restores uniformity. The resulting TiOH/PVA–Nafion multilayer DBRs exhibit smooth interfaces and highly regular periodicity, as confirmed by the cross-sectional SEM shown in Fig. 32(b). The specific processing parameters used in this thesis are summarised in Table 4.

Table 4. Dip-coating parameters used for the fabrication of dielectric DBR layers in this thesis.

Material	Solvent / Host	Conc. (mg/mL)	Withdrawal speed	Annealing
TiOH/PVA	Water / PVA	22	40 mm/min	80°C / 1 min
Nafion	IPA	XX	40 mm/min	80°C / 1 min

6.3 Optical Characterisation

6.3.1 Fourier-space (k-space) and real-space microspectroscopy

A versatile optical microscope–spectroscopy platform was employed throughout this thesis to perform real-space imaging, and k-space (Fourier-plane) spectroscopy for reflectivity and PL of the samples. The same setup was used in Publications I and II for reflectivity measurements, in Publication III for polariton PL and nonlinear emission studies and in Publication IV and V for polariton EL studies.

Principle of k-space spectroscopy. Fourier-space spectroscopy exploits the angular information encoded in the far-field (FF) emission or reflection of a sample. In an infinity-corrected microscope, the microscope objective maps each emission angle onto a unique position in its back focal plane (BFP), such that the BFP represents the angular—or equivalently momentum—distribution of the emitted light. The center of the BFP corresponds to normal emission ($\theta = 0°$), while the radial coordinate represents increasing emission angle up to the maximum collection angle defined by the numerical aperture (NA) of the objective.

Because the magnitude of the photon wavevector in a medium of refractive index n is $k = n\omega/c$, the in-plane momentum component is given by

$$k_{\parallel} = \frac{n\omega}{c} \sin\theta,$$

establishing a direct correspondence between emission angle and in-plane momentum. Consequently, imaging the BFP provides direct access to the momentum-space distribution of the optical modes.

In the Fourier-space configuration, the BFP is projected onto the entrance slit of an imaging spectrometer. When the slit is nearly closed, a narrow cut through the Fourier plane is selected, corresponding to a fixed transverse momentum component (typically $k_y \approx 0$), while the orthogonal direction is spectrally dispersed by the grating. This configuration yields two-dimensional energy–momentum (E–$k_{\parallel}$) spectra, where each pixel row corresponds to a distinct in-plane momentum value. Such measurements enable direct visualization of cavity and polariton dispersions, identification of anticrossings, and extraction of key parameters including linewidths, detunings, and Rabi splittings.

Optical layout. Angle-resolved reflectivity measurements were performed using a broadband white-light source (Thorlabs SLS201). For photoluminescence (PL) excitation, a Light Conversion Pharos femtosecond laser system, coupled to Orpheus and Lyra OPA, provided tunable excitation wavelengths spanning 280–2500 nm. Excitation and collection were performed through the same optical path using infinity-corrected microscope objectives with numerical apertures ranging from 0.2 to 0.75, depending on the measurement.

A beamsplitter positioned in front of the objective enabled coaxial illumination for reflectivity measurements while preserving efficient signal collection. Light emitted or reflected from the sample exits the objective as a collimated beam and is imaged by a 200 mm tube lens. A secondary beamsplitter directs a fraction of this beam to a CMOS camera for real-space imaging, sample alignment, and monitoring during measurements.

The remaining beam is routed to the spectroscopy arm, where relay optics project either the real-space image or the objective back focal plane onto the entrance slit of an imaging spectrometer (Teledyne Pixis 400) equipped with a two-dimensional CCD detector (1340 $\times$ 400 pixels). In the Fourier-space configuration, the objective back focal plane is imaged onto the entrance slit of the spectrometer for angle-resolved reflectivity and PL measurements. Interchangeable gratings provide spectral dispersion for energy–momentum mapping, while time-resolved measurements are performed by redirecting the spectrometer output to Timeharp-260 avalanche photodiode (APD).

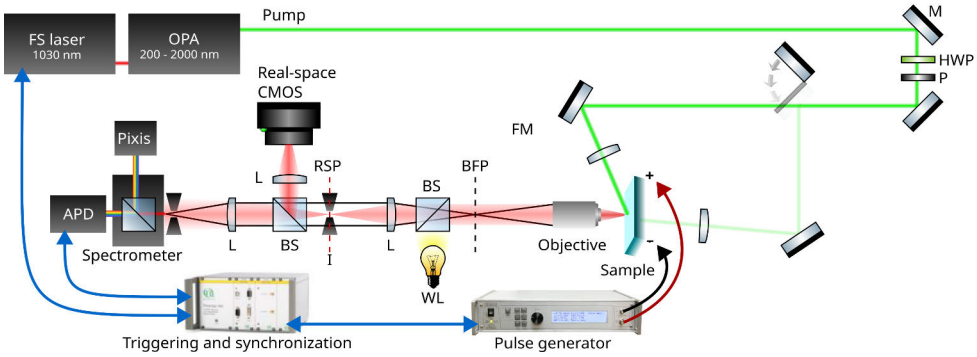

Figure 33. Schematic of the real-space and k-space microspectroscopy setup used for angle-resolved reflectivity and photoluminescence measurements. The objective and tube lens provide real-space imaging, while appropriate relay optics project either the real-space plane or the back focal plane onto the spectrometer entrance slit. A white-light source is injected through a beamsplitter for reflectivity, and PL is collected under non-resonant OPA excitation. Detection is performed via a CMOS camera (imaging), CCD (spectroscopy), or APD (time-resolved measurements).

6.3.2 Ellipsometry

Spectroscopic ellipsometry was employed extensively in this thesis to characterise the optical properties and thicknesses of thin films used in both the solution-processed and vacuum-deposited microcavities. Measurements were performed using a VASE ellipsometer covering the spectral range 193-3000 nm.

Ellipsometry measures the complex reflectance ratio

$$\rho = \frac{r_p}{r_s} = \tan(\Psi)\, e^{i\Delta},$$

where Ψ and Δ describe the change in amplitude and phase of p- and s-polarised light upon reflection. By modelling the measured (Ψ, Δ) spectra, material parameters such as film thickness, refractive index $n(\lambda)$, and extinction coefficient $k(\lambda)$ can be extracted with high accuracy.

Thickness determination. For organic and polymer films exhibiting negligible absorption in a transparent spectral region, thicknesses were obtained by fitting the data with a Cauchy dispersion model of the form

$$n(\lambda) = A + \frac{B}{\lambda^2} + \frac{C}{\lambda^4}, \qquad k(\lambda) = 0,$$

which reliably describes transparent dielectric films. This method was used to determine the thicknesses of all the spin coated, dip coated and thermally evaporated films in all the publications included in this thesis.

Extraction of optical constants. For films exhibiting absorption in the visible spectral range—such as the TiOH/PVA hybrid layers or optically active organic emitters—the refractive index and extinction coefficient were retrieved by fitting the ellipsometric data with a Tauc-Lorentz oscillator model. This physically motivated model combines a Tauc joint density of states with Lorentz oscillators, allowing a self-consistent description of both interband absorption and the real part of the dielectric function. The extracted $n(\lambda)$ and $k(\lambda)$ values were used as inputs for TMM simulations of the microcavities.

7 Conclusions and future outlook

This thesis has investigated optical microcavities and strong light–matter coupling in organic systems, with a particular emphasis on solution-processed fabrication routes, their optical performance, and their implications for polaritonic devices. By combining scalable fabrication strategies with detailed optical and spectroscopic characterization, this work demonstrates that high-quality microcavities and polaritonic phenomena are not inherently restricted to vacuum-based processing.

Publication I, a solution-processed distributed Bragg reflector (DBR) platform based on alternating Nafion and TiOH/PVA layers was introduced. Using an automated dip-coating approach, sub-100-nm multilayers with good thickness control and reproducibility were achieved, enabling both hybrid DBR/metal and fully dielectric microcavities. Despite the use of only six DBR pairs, quality factors exceeding 90 were obtained, highlighting the effectiveness of the approach. The use of Nafion as a low-index material provided a cost-effective alternative to fluorinated polymers commonly used in solution-processed DBRs. While the limited availability of purely polymeric high-index materials remains a challenge, this work establishes solution-processed DBRs as a viable and scalable route for organic microcavity fabrication.

Building on this platform, Publication II demonstrated strong light–matter coupling in a fully solution-processed dielectric microcavity incorporating Rhodamine 6G as the active material. Large Rabi splittings exceeding 400 meV were achieved, together with clear lower-polariton photoluminescence. Importantly, the coupling strengths matched or surpassed those obtained in comparable metal-clad microcavities, confirming that solution-processed dielectric cavities can reach the strong-coupling regime without compromising optical quality. Excitation-dependent measurements revealed a suppression of singlet–singlet annihilation in the polaritonic structures compared to bare films, emphasizing the role of strong coupling and cavity-modified optical environments in shaping photophysical observables. Beyond the specific material system studied, this work lowers the experimental barrier to entry for polariton research by combining accessible fabrication and characterization techniques.

In Publication III, the solution-processed platform was extended to demonstrate the first fully solution-processed organic polariton microcavity laser. Both the dielectric mirrors and the DPAVB:PS active layer were fabricated by spin coating, enabling rapid, low-energy-cost device fabrication. Beyond the technical achieve-

ment, this system revealed new polariton condensation behavior, including a reversible annular redistribution of the condensate under Gaussian excitation and signatures of enhanced polariton–polariton scattering at high excitation densities. The observed thermalization of the high-energy tail of the emission indicates efficient energy redistribution within the polariton system. While the microscopic origin of these effects warrants further investigation, the results highlight how simple fabrication routes combined with tailored material choices can unlock qualitatively new polariton physics.

Publication IV addressed the impact of strong coupling on excitonic relaxation dynamics in electrically driven organic devices. By comparing polaritonic OLEDs (POLEDs) with non-cavity reference OLEDs and tuning the lower polariton mode relative to molecular triplet energies, no significant modification of delayed electroluminescence dynamics was observed. Rate-equation modelling showed that the delayed emission originated from charge trapping rather than polariton-mediated triplet harvesting. These results demonstrate that, for the studied TADF system, strong coupling does not provide a straightforward route to modifying triplet management. At the same time, the work highlights the importance of carefully distinguishing photonic effects from genuine changes in molecular kinetics and identifies clear experimental boundaries for polaritonic control of excited-state processes.

Finally, Publication V explored photonic microcavity effects in metal-clad white OLEDs, focusing on spectral engineering rather than strong coupling. A simplified WOLED architecture was demonstrated using a single-component DMAC-DPS emitting layer and eliminating the need for ITO electrodes. White emission was achieved through the combined action of cavity modes and surface plasmon polaritons at the metal interface, with tunable correlated color temperature controlled by cavity thickness. Optical simulations based on classical dipole emission and transfer-matrix modelling reproduced the experimental spectra and confirmed that the observed effects originate from cavity-engineered photonic density of states. While device efficiencies remain below those of optimized reference OLEDs, this work demonstrates the potential of microcavity photonics for spectrally engineered, low-complexity lighting devices.

The results presented in this thesis demonstrate that solution-processed microcavities can support not only strong light–matter coupling but also nonlinear polaritonic phenomena, including polariton lasing. This establishes solution processing as a viable and scalable route for realizing advanced polaritonic architectures under ambient conditions. However, while polariton lasing represents a significant milestone, its translation into practical optoelectronic device concepts—particularly electrically driven devices such as OLEDs—remains an open challenge.

From a materials perspective, further progress in solution-processed high-refractive-index layers—ideally based on purely polymeric systems—could reduce scattering losses and improve optical quality, enabling higher-Q dielectric mirrors with fewer

layer pairs. Such developments would directly benefit both polaritonic devices and photonic microcavity OLED architectures. In parallel, replacing fluorinated low-index layers such as Nafion with more environmentally benign alternatives will be important for sustainable scale-up of solution-processed DBRs.

Finally, the solution-processed polariton platform introduced here opens opportunities to explore nonequilibrium polariton dynamics, thermalization, and interaction effects in organic systems using accessible fabrication and characterization techniques. Systematic studies combining improved cavity designs with spatially and temporally resolved spectroscopy may clarify the conditions under which polaritonic states can offer tangible advantages for optoelectronic applications.

List of References

[1] Alexey Kavokin, Jeremy J. Baumberg, Guillaume Malpuech, and Fabrice P. Laussy. *Microcavities*. Oxford University Press, 2017.

[2] Serge Haroche and Jean-Michel Raimond. *Exploring the Quantum: Atoms, Cavities, and Photons*. Oxford University Press, 2006.

[3] James Clerk Maxwell. Viii. a dynamical theory of the electromagnetic field. *Philosophical Transactions of the Royal Society of London*, (155):459–512, 12 1865.

[4] H. Hertz. Ueber sehr schnelle electrische schwingungen. *Annalen der Physik*, 267(7):421–448, 1887.

[5] A. Einstein. Über einen die erzeugung und verwandlung des lichtes betreffenden heuristischen gesichtspunkt. *Annalen der Physik*, 322(6):132–148, 1905.

[6] Max Planck. Ueber das gesetz der energieverteilung im normalspectrum. *Annalen der Physik*, 309(3):553–563, 1901.

[7] Paul Adrien Maurice Dirac. The quantum theory of the emission and absorption of radiation. *Proceedings of the Royal Society of London. Series A, Containing Papers of a Mathematical and Physical Character*, 114(767):243–265, 03 1927.

[8] Werner Heisenberg. Über den anschaulichen inhalt der quantentheoretischen kinematik und mechanik. *Zeitschrift für Physik*, 43(3):172–198, 1927.

[9] C. Weisbuch, M. Nishioka, A. Ishikawa, and Y. Arakawa. Observation of the coupled exciton-photon mode splitting in a semiconductor quantum microcavity. *Phys. Rev. Lett.*, 69:3314–3317, Dec 1992.

[10] V. Savona, L. C. Andreani, P. Schwendimann, and A. Quattropani. Quantum well excitons in semiconductor microcavities: Unified treatment of weak and strong coupling regimes. *Solid State Communications*, 1995.

[11] David G. Lidzey, Donal D. C. Bradley, Maurice S. Skolnick, Salt Walker, David M. Whittaker, and Jeremy J. Baumberg. Strong exciton-photon coupling in an organic semiconductor microcavity. *Nature*, 395:53–55, 1998.

[12] Hui Deng, Hartmut Haug, and Yoshihisa Yamamoto. Exciton-polariton bose-einstein condensation. *Reviews of Modern Physics*, 82(2):1489–1537, 2010.

[13] D. Polak, R. Jayaprakash, T. P. Lyons, and et al. Manipulating molecules with strong coupling: Harvesting triplet excitons in organic exciton microcavities. *Chemical Science*, 11(2):343–354, 2020.

[14] Edwin T. Jaynes and Frederick W. Cummings. Comparison of quantum and semiclassical radiation theories with application to the beam maser. *Proceedings of the IEEE*, 1963.

[15] Serge Haroche et al. Cavity quantum electrodynamics. *Physics Today*, 42(1):24–30, 1989.

[16] R. Houdré, C. Weisbuch, R. P. Stanley, U. Oesterle, P. Pellandini, and M. Ilegems. Measurement of cavity-polariton dispersion curve from angle-resolved photoluminescence experiments. *Phys. Rev. Lett.*, 73:2043–2046, Oct 1994.

[17] Y. Kaluzny, P. Goy, M. Gross, J. M. Raimond, and S. Haroche. Observation of self-induced rabi oscillations in two-level atoms excited inside a resonant cavity: The ringing regime of superradiance. *Phys. Rev. Lett.*, 51:1175–1178, Sep 1983.

[18] V. Agranovich, H. Benisty, and C. Weisbuch. Organic and inorganic quantum wells in a microcavity: Frenkel-wannier-mott excitons hybridization and energy transformation. *Solid State Communications*, 102(8):631–636, 1997.

[19] A. Imamoğlu, R. J. Ram, S. Pau, and Y. Yamamoto. Nonequilibrium condensates and lasers without inversion: Exciton–polariton lasers. *Physical Review A*, 53(6):4250–4253, 1996.

[20] S. Christopoulos, G. B. H. von Högersthal, A. J. D. Grundy, P. G. Lagoudakis, A. V. Kavokin, J. J. Baumberg, G. Christmann, R. Butté, E. Feltin, J.-F. Carlin, and N. Grandjean. Room-temperature polariton lasing in semiconductor microcavities. *Physical Review Letters*, 98:126405, 2007.

[21] G. Christmann, R. Butté, E. Feltin, J.-F. Carlin, and N. Grandjean. Room temperature polariton lasing in a gan–algan multiple quantum well microcavity. *Applied Physics Letters*, 93:051102, 2008.

[22] Stéphane Kéna-Cohen and Stephen R. Forrest. Room-temperature polariton lasing in an organic single-crystal microcavity. *Nature Photonics*, 2010.

[23] Anna Köhler and Heinz Bässler. *Electronic Processes in Organic Semiconductors*. Wiley-VCH, 2015.

[24] Rahul Bhuyan, Jürgen Mony, Oleg Kotov, Gabriel W. Castellanos, Jaime Gómez Rivas, Timur O. Shegai, and Karl Börjesson. The rise and current status of polaritonic photochemistry and photophysics. *Chemical Reviews*, 123(18):10877–10919, 2023. PMID: 37683254.

[25] Russell J. Holmes and Stephen R. Forrest. Strong exciton-photon coupling and exciton hybridization in a multiple quantum well organic semiconductor microcavity. *Physical Review Letters*, 93(18):186404, 2004.

[26] J. D. Plumhof, T. Stöferle, L. Mai, U. Scherf, and R. F. Mahrt. Room-temperature bose–einstein condensation of cavity exciton–polaritons in a polymer. *Nature Materials*, 13:247–252, 2014.

[27] Paola Lova, Giovanni Manfredi, and Davide Comoretto. Advances in functional solution processed planar 1d photonic crystals. *Advanced Optical Materials*, 6(24):1800730, 2018.

[28] Andrew Strang, Victoria Quirós-Cordero, Pascal Grégoire, Sara Pla, Fernando Fernández-Lázaro, Ángela Sastre-Santos, Carlos Silva-Acuña, Paul N. Stavrinou, and Natalie Stingelin. Simple and versatile platforms for manipulating light with matter: Strong light–matter coupling in fully solution-processed optical microcavities. *Advanced Materials*, 36(20):2212056, 2024.

[29] Emilia Palo, Michael A. Papachatzakis, Ahmed Abdelmagid, Hassan Qureshi, Manish Kumar, Mikko Salomäki, and Konstantinos S. Daskalakis. Developing solution-processed distributed bragg reflectors for microcavity polariton applications. *The Journal of Physical Chemistry C*, 127(29):14255–14262, 2023.

[30] Hassan A. Qureshi, Michael A. Papachatzakis, Ahmed Gaber Abdelmagid, Mikko Salomäki, Ermei Mäkilä, Oskar Tuomi, Olli Siltanen, and Konstantinos S. Daskalakis. Giant rabi splitting and polariton photoluminescence in an all solution-deposited dielectric microcavity. *Advanced Optical Materials*, 13(16):2500155, 2025.

[31] Manish Kumar, Arpan Dutta, Hassan A. Qureshi, Michael A. Papachatzakis, Ahmed Gaber Abdelmagid, and Konstantinos S. Daskalakis. Single-emitter white oleds via microcavity spectral engineering. *Advanced Optical Materials*, 13(28):e01358, 2025.

[32] J. A. Hutchison et al. Modifying chemical landscapes via strong light–matter coupling. *Angewandte Chemie*, 51:1592–1596, 2012.

[33] T. W. Ebbesen. Hybrid light–matter states in a molecular and material science perspective. *Accounts of Chemical Research*, 49:2403–2412, 2016.

[34] K. Stranius, M. Hertzog, and K. Börjesson. Selective manipulation of electronically excited states through strong light–matter interactions. *Nature Communications*, 9:2273, 2018.

[35] L. A. Martínez-Martínez, M. Du, R. F. Ribeiro, S. Kéna-Cohen, and J. Yuen-Zhou. Polariton-assisted singlet fission in acene aggregates. *The Journal of Physical Chemistry Letters*, 9:1951–1957, 2018.

[36] A. M. Berghuis, A. Halpin, Q. Le-Van, and et al. Enhanced delayed fluorescence in tetracene crystals by strong light–matter coupling. *Advanced Functional Materials*, 29:1901317, 2019.

[37] E. Eizner, L. A. Martínez-Martínez, J. Yuen-Zhou, and S. Kéna-Cohen. Inverting singlet and triplet excited states using strong light–matter coupling. *Science Advances*, 5:eaax4482, 2019.
[38] Y. Yu, S. Mallick, M. Wang, and K. Börjesson. Barrier-free reverse-intersystem crossing in organic molecules by strong light–matter coupling. *Nature Communications*, 12:1–8, 2021.
[39] A. Mukherjee, J. Feist, and K. Börjesson. Quantitative investigation of the rate of intersystem crossing in the strong exciton–photon coupling regime. *Journal of the American Chemical Society*, 145:5155–5162, 2023.
[40] Eugene Hecht. *Optics*. Pearson Education, 2017.
[41] Orazio Svelto. *Principles of Lasers*. Springer, 2010.
[42] Larry A. Coldren, Steven W. Corzine, and Milan L. Mashanovitch. *Diode Lasers and Photonic Integrated Circuits*. Wiley, 2012.
[43] Daniele Sanvitto and Stéphane Kéna-Cohen. The road towards polaritonic devices. *Nature Materials*, 2016.
[44] P. B. Johnson and R. W. Christy. Optical constants of the noble metals. *Physical Review B*, 1972.
[45] K. M. McPeak, S. V. Jayanti, S. J. P. Kress, S. Meyer, S. Iotti, A. Rossinelli, and D. J. Norris. Plasmonic films can easily be better: Rules and recipes. *ACS Photonics*, 2015.
[46] S. Bachevillier. *Solution-Processed Photonics for Light and Heat Management*. Ph.d. dissertation, Imperial College London, 2018.
[47] M. J. Seitz and P. M. Horkans. Nafion: Properties, structure and applications. *ResearchGate*, 2018. Accessed: 2025-12-16.
[48] Arash Rahimi-Iman. *Polariton Physics*. Springer, 2020.
[49] Stephen R. Forrest. *Organic Electronics: Foundations to Applications*. Oxford University Press, 2020.
[50] Martin Pope and Charles E. Swenberg. *Electronic Processes in Organic Crystals and Polymers*. Oxford University Press, 1999.
[51] Marc A. Baldo, D. F. O'Brien, Y. You, A. Shoustikov, S. Sibley, Mark E. Thompson, and Stephen R. Forrest. Highly efficient phosphorescent emission from organic electroluminescent devices. *Nature*, 1998.
[52] Hiroki Uoyama, Kenichi Goushi, Katsuyuki Shizu, Hiroyuki Nomura, and Chihaya Adachi. Highly efficient organic light-emitting diodes from delayed fluorescence. *Nature*, 2012.
[53] Jean-Michel Gérard and Bruno Gayral. Strong purcell effect in semiconductor microcavities. *Journal of Lightwave Technology*, 1998.
[54] Edward M. Purcell. Spontaneous emission probabilities at radio frequencies. *Physical Review*, 1946.
[55] Serge Haroche and Jean-Michel Raimond. *Exploring the Quantum: Atoms, Cavities, and Photons*. Oxford University Press, 2006.
[56] J. J. Hopfield. Theory of the contribution of excitons to the complex dielectric constant of crystals. *Physical Review*, 1958.
[57] Konstantinos S. Daskalakis, Stefan A. Maier, Ray F. Murray, and Stéphane Kéna-Cohen. Nonlinear interactions in an organic polariton condensate. *Nature Materials*, 2014.
[58] C. P. Dietrich, A. Steude, L. Tropf, M. Schubert, N. M. Kronenberg, K. Ostermann, S. Höfling, and Malte C. Gather. An exciton-polariton laser based on biologically produced fluorescent protein. *Science Advances*, 2016.
[59] K. Yamashita, U. Huynh, J. Richter, L. Eyre, F. Deschler, A. Rao, K. Goto, T. Nishimura, T. Yamao, S. Hotta, H. Yanagi, M. Nakayama, and R. H. Friend. Ultrafast dynamics of polariton cooling and renormalization in an organic single-crystal microcavity under nonresonant pumping. *ACS Photonics*, 2018.
[60] Stefan A. Maier. *Plasmonics: Fundamentals and Applications*. Springer, 2007.
[61] Paivi Törmä and William L. Barnes. Strong coupling between surface plasmon polaritons and emitters: a review. *Reports on Progress in Physics*, 2015.
[62] Joshua D. Caldwell, Lucas Lindsay, Vincenzo Giannini, and et al. Low-loss, infrared and terahertz nanophotonics using surface phonon polaritons. *Nanophotonics*, 2015.

[63] Hui Deng, G. Weihs, C. Santori, J. Bloch, and Y. Yamamoto. Condensation of semiconductor microcavity exciton polaritons. *Science*, 2002.

[64] J. Kasprzak, M. Richard, S. Kundermann, A. Baas, P. Jeambrun, J. M. J. Keeling, F. M. Marchetti, M. H. Szymańska, R. André, J. L. Staehli, V. Savona, P. B. Littlewood, B. Deveaud, and L. S. Dang. Bose–einstein condensation of exciton polaritons. *Nature*, 2006.

[65] Tim Byrnes, Na Kim, and Yoshihisa Yamamoto. Exciton–polariton condensates. *Nature Physics*, 2014.

[66] Iacopo Carusotto and Cristiano Ciuti. Quantum fluids of light. *Reviews of Modern Physics*, 2013.

[67] Alberto Tosi, Paolo Cristofolini, and et al. Geometrically locked vortex lattices in semiconductor quantum fluids of light. *Nature Communications*, 2012.

[68] R. H. Friend, R. W. Gymer, et al. Electroluminescence in conjugated polymers. *Nature*, 397:121–128, 1999.

[69] S. Reineke et al. White organic light-emitting diodes with fluorescent tube efficiency. *Nature*, 459:234–238, 2009.

[70] S. R. Forrest. The path to ubiquitous and low-cost organic electronic appliances. *Nature*, 428:911–918, 2003.

[71] M. C. Gather et al. Light management in oleds. *Advanced Materials*, 23:233–248, 2011.

[72] C. W. Tang and S. A. VanSlyke. Organic electroluminescent diodes. *Applied Physics Letters*, 51:913–915, 1987.

[73] T. Tsutsui. Recent progress in high-efficiency organic light-emitting devices. *MRS Bulletin*, 26:108–113, 2001.

[74] J.-L. Brédas et al. Photophysics of organic semiconductors. *Advanced Materials*, 21:1–22, 2009.

[75] H. Uoyama et al. Highly efficient organic light-emitting diodes from delayed fluorescence. *Nature*, 492:234–238, 2012.

[76] A. Endo et al. Efficient up-conversion of triplet excitons into a singlet state via risc. *Applied Physics Letters*, 98:083302, 2011.

[77] H. Yersin. Highly efficient oleds with phosphorescent materials. *Topics in Current Chemistry*, 325:1–26, 2011.

[78] M. Lu et al. Metal–dielectric microcavity engineering of oled emission. *Light: Science & Applications*, 3:e193, 2014.

[79] Martin Pope and Charles E. Swenberg. *Electronic Processes in Organic Crystals and Polymers*. Oxford University Press, 1999.

[80] J. Brooks et al. Understanding nonradiative pathways in organic emitters. *Chemistry of Materials*, 30:3663–3675, 2018.

[81] M. Wohlgenannt et al. Spin-dependent exciton formation rates in conjugated polymers. *Nature*, 409:494–497, 2001.

[82] Joseph R. Lakowicz. *Principles of Fluorescence Spectroscopy*. Springer, 2006.

[83] Johannes Gierschner, Thomas J. Penfold, and Yoann Olivier. Organic luminescent materials: Theoretical understanding of excited-state processes. *Journal of Chemical Physics*, 2013.

[84] Denis Y. Kondakov, William C. Lenhart, and William F. Nichols. Operational stability of organic light-emitting diodes: Mechanism and effect of electron transport layer. *Journal of Applied Physics*, 2007.

[85] V. Russo, M. Fittipaldi, G. Nicotra, and C. Spinella. Hydrolysis and condensation processes of ticl4-derived titanium oxide hydrates. *Chemistry of Materials*, 2007.

[86] Stefan Bachevillier, Hua-Kang Yuan, Andrew Strang, Artem Levitsky, Gitti L. Frey, Andreas Hafner, Donal D. C. Bradley, Paul N. Stavrinou, and Natalie Stingelin. Fully solution-processed photonic structures from inorganic/organic molecular hybrid materials and commodity polymers. *Advanced Functional Materials*, 2019.

TURUN
YLIOPISTO
UNIVERSITY
OF TURKU

Painosalama, Turku, Finland 2026

ISBN 978-952-02-0621-5 (PRINT)
ISBN 978-952-02-0622-2 (PDF)
ISSN 2736-9390 (PRINT)
ISSN 2736-9684 (ONLINE)